Airborne Geophysical Analysis to Decipher Salinization for Coastal Louisiana

Michael Attia[1], Frank T.-C. Tsai[1,*], Shuo Yang[2], Burke Minsley[3], Wade H. Kress[4]

[1]Department of Civil and Environmental Engineering, Louisiana State University, Baton Rouge, Louisiana, 70803, Email: mattia1@lsu.edu; ftsai@lsu.edu

[2]INTERA Incorporated, Austin, TX 78759; syang@intera.com (Formerly, Department of Civil and Environmental Engineering, Louisiana State University)

[3]U.S. Geological Survey, Geology, Geophysics, and Geochemistry Science Center, Denver, CO 80225, Email: bminsley@usgs.gov

[4]U.S. Geological Survey, Lower Mississippi-Gulf Water Science Center, Nashville, TN 37211, Email: wkress@usgs.gov

*Corresponding author: Frank Tsai (ftsai@lsu.edu)

Highlights

- Airborne electromagnetic (AEM) surveys delineate salinity for wetlands and aquifers.
- AEM data reveals saltwater intrusion to aquifers from deep depths and the Gulf.
- Dramatic changes in AEM-inferred salinity suggest the presence of faults.
- AEM data reveals seawater intrusion into the Mississippi and Atchafalaya Rivers.

Abstract

Coastal Louisiana is known for saltwater intrusion that threatens wetlands, aquifers, and rivers. However, the extent of saltwater intrusion is not well understood. This study develops an innovative framework with airborne electromagnetic (AEM) data to map chloride concentration distributions for wetlands in the Mississippi River deltaic plain and Chenier plain as well as for the Mississippi River Valley alluvial aquifer (MRVA) and Chicot aquifer. Moreover, the framework maps chloride concentrations along the Mississippi River and Atchafalaya River. Key components in the framework include the establishment of resistivity-to-chloride concentration transformation, 3D resistivity architecture building through geostatistics, and the employment of a lithologic model. The transformation functions correlate AEM resistivity data with porewater salinity measurements and groundwater and river chloride samples. The results show that AEM data reliably infers soil water chloride concentrations and correlates well with the distribution of various marsh types. AEM data reveals extensive saltwater presence at depth and near the coast, originating from salt domes and the Gulf of Mexico, respectively. The saltwater upconing pattern in the Chicot aquifer is likely due to excessive groundwater withdrawals. The AEM data also confirms a distinct tongue of saltwater intruding into the Atchafalaya Basin from the Gulf. The AEM data helps to identify faults that are obscured or eroded at the surface, which appear as leaky barriers in the subsurface where dramatic changes in chloride concentration are apparent. Finally, this study uses the AEM data to infer the presence of an extensive seawater wedge in the Mississippi River and Atchafalaya River.

Keywords: Airborne electromagnetic survey, saltwater intrusion, wetland, aquifer, river, fault.

1. Introduction

Over one-third of the world's population lives within 100 km of the coast (Reimann et al., 2023), highlighting the importance of coastal wetlands and groundwater resource protection. Coastal areas worldwide experience dynamic interactions between freshwater and saltwater (Goebel et al., 2019). Salinity is an important factor in structuring coastal wetland communities and influencing biogeochemical pathways (Baustian et al., 2017; Craft et al., 2009). However, seawater intrusion and changes in salinity due to sea level rise and land subsidence can diminish freshwater marshes (Li et al., 2018; Neubauer et al., 2013).

The intrusion of saltwater into coastal aquifers is becoming more challenging for coastal communities worldwide, affecting drinking water supply, crop irrigation, and industries. Coastal aquifers are vulnerable to atmospheric climate change and sea-level rise because both potentially impact saltwater intrusion (Rasmussen et al., 2013). Over-pumping of freshwater can exacerbate saltwater intrusion as pumping reduces the natural hydraulic gradient to the sea which can cause the saltwater-freshwater interface to move inland (Klassen & Allen, 2017; Panthi et al., 2022). Also, over-pumping can lead to upconing of deep saline waters to shallower aquifers (Jasechko et al., 2020; Panthi et al., 2022). Top-down seawater intrusion can occur in coastal zones due to tsunamis, storm surges, extreme high tides, high-amplitude waves, or a combination of these factors (Bilskie et al., 2014).

Coastal Louisiana's groundwater salinization is influenced by seawater from the gulf and paleo saltwater from salt domes and is interrupted by fault systems. The fault systems, including the Tepetate-Baton Rouge fault system, can function as conduits and barriers (Bense & Person, 2006) and disrupt saltwater movement across fault planes (Elshall et al., 2013; Pham and Tsai 2017). Paleo saltwater dissolved from salt domes (Beckman & Williamson, 1990) is the major

source of salt present at deep depths. Pumping activities in the coastal region can exacerbate paleo saltwater upconing into shallow depths.

Mapping and monitoring the subsurface distribution of salinity is imperative for managing coastal wetlands and groundwater resources. Traditional salinity mapping is accomplished through water sample collection. However, water samples are often sparse, except for a few relatively small and highly characterized areas (Schiavo et al., 2023). Sparse data and limited coverage often result in higher uncertainty in maps of salinity. However, airborne electromagnetic (AEM) surveying has the potential to expand limited salinity measurements into large-scale saltwater plume delineation, shifting from borehole-based to regionally distributed information. AEM, as a geophysical technique, is useful for developing subsurface models that accurately delineate the distribution of aquifers and aquitards, saltwater and freshwater interfaces, and geological structures that influence groundwater flow (Jørgensen et al., 2012). AEM provides a measure of subsurface electrical resistivity, which is highly sensitive to changes in pore fluid salinity and is an effective way to map groundwater salinity. The first successful application of AEM surveys to map saline areas was in the late 1970s (Sengpiel and Meiser, 1981). Since then, AEM has proven to be highly effective in visualizing the subsurface and extensively exploring and assessing saltwater intrusion in coastal areas (Goebel et al., 2019; Gottschalk et al., 2020). AEM has increasingly been used as a tool for characterizing the subsurface because it is rapid, non-invasive, and cost-effective, especially when mapping salinity over large areas (Attia and Tsai, 2024a). Compared to more standard EM approaches, such as terrestrial above-ground surveys or down-well logging, AEM provides broader spatial coverage and does not require direct ground access, making it particularly advantageous for mapping salinity in remote or inaccessible areas. Nevertheless, standard EM methods can provide high-resolution data at specific locations.

Relying solely on the measurement of electrical resistivity to indicate water salinity can be misleading and challenging. The electrical resistivity of subsurface materials is influenced not only by water salinity, but also by the texture and minerals of sediments, and the volume of water present (Gottschalk et al., 2020). For instance, clay-rich sediments and saltwater have lower resistivity (high conductivity) values than coarse-grained or freshwater counterparts (Attia and Tsai, 2024a). This underscores the importance of mapping subsurface lithology to distinguish saline aquifers from aquitards to determine the relationship between AEM resistivity and salinity.

The challenges of mapping salinity are further compounded when considering the interactions between groundwater and surface water, particularly in riverine environments (Lane et al., 2020). The physical structure and permeability of riverbeds play a crucial role in groundwater/surface water (GW/SW) exchanges, which significantly affect water quality (Bianchin et al., 2011; Boano et al., 2014). Waterborne and airborne electromagnetic mapping techniques have demonstrated effectiveness in assessing salinity in surface waters (Hatch et al., 2010; Paine et al., 2009). These methods offer rapid and extensive coverage, making them superior to traditional sampling approaches that are often impractical on large scales (Kalbus et al., 2006; Briggs et al., 2019).

The objective of this study is to investigate the salinity distribution in Louisiana's coastal zone. The novelty of this study lies in the integration of AEM data along with water quality data and lithologic modeling to comprehensively estimate salinity in wetlands, aquifers, and rivers, which has not been previously achieved at this scale. The results map salinity conditions for the coastal wetlands in the Mississippi River deltaic plain and Chenier plain, and also for the Mississippi River Valley alluvial aquifer and Chicot aquifer. In addition, this study delineates the seawater wedges in the Mississippi River and Atchafalaya River and infers fault traces as leaky

barriers. This study advances the understanding of coastal salinization by providing detailed 3D salinity mapping, a significant improvement over previous methods that have been limited in spatial resolution and integration of diverse data sources.

2. Study Area: Louisiana's Coastal Zone

The study area is in south Louisiana, adjacent to the Gulf of Mexico. The study area covers 63,457 km^2 and comprises 27 parishes as shown in Fig. 1. The major Holocene landforms include the Mississippi River deltaic plain, the Chenier plain, and the Atchafalaya Basin. Within the study area, Pleistocene deposits are exposed at the surface in southwestern Louisiana. The Mississippi River deltaic plain is located along the eastern shoreline, where the coastal morphology is a product of sediment deposition. It is also the present location of the Mississippi River Delta (Oliver-Cabrera & Wdowinski, 2016). The late Holocene Chenier plain is located along the western part of the shoreline, where the coastline's morphology consists of wooded beach ridges and mudflats covered by swamps and marshes (McBride et al., 2007). The Atchafalaya Basin contains the Atchafalaya River and covers the southernmost part of the Mississippi Alluvial Plain (Ladd and Travers, 2019). The groundwater dynamics from 2004-2021 in the study area was studied, including the MRVA and the Chicot aquifer, through a statewide 3D high-resolution groundwater flow model developed by Yang et al. (2023). Groundwater levels are generally near the land surface in the low-lying wetlands and several meters below the land surface in the heavily pumped areas in southwest Louisiana. In other words, the vadose zone in the coastal Louisiana is limited. The groundwater model aids this study in understanding the connections between saltwater intrusion and groundwater levels.

2.1. Wetlands and Salinization Impact

Louisiana's coastal wetlands cover 40% of the U.S. coastal wetlands, extending 130 km inland and 300 km along the coast and encompassing around 37,780 km² of lowland plains, deltaic lobes, and open water (Couvillion et al., 2017). These wetlands provide crucial ecosystem services such as wildlife habitat, storm protection, flood control, water storage, erosion reduction, carbon sequestration, fisheries support, water quality improvement, and recreational opportunities (Barbier et al., 2011; Oliver-Cabrera & Wdowinski, 2016). Vegetation varies with salinity conditions and includes salt, brackish, intermediate, and freshwater marshes, as well as swamps in freshwater zones (Nyman et al. 2022; Oliver-Cabrera & Wdowinski, 2016).

Louisiana's coastal wetlands are among the nation's most fragile ecosystems due to sea level rise, subsidence, seawater intrusion, and infrastructure development. Louisiana coastal wetlands lost about 25% of their land area from 1932 to 2016 (Couvillion et al., 2017). Increasing salinity from saltwater intrusion has led to wetland change and loss, with saline marshes expanding inland and fresh/brackish marshes contracting. Reduced sediment delivery and saltwater exposure make these wetlands less capable of combating sea level rise.

2.2. Aquifers and Saltwater Presence

Fresh groundwater in the study area mainly exists in the two regional hydrogeologic units: the Mississippi River Valley alluvial aquifer (MRVA) and the Chicot aquifer. The MRVA extends from south Illinois down to the Gulf (Ladd & Travers, 2019), overlain by a surficial confining unit. The MRVA in Louisiana is often referred to as the Mississippi River alluvial aquifer, which underlies the Atchafalaya Basin and the western part of the deltaic plain. The Chicot aquifer contains thick sand and gravel deposits of Pleistocene and consists of sands interbedded with clays

or sands separated by extensive confining units (Lindaman, 2023). The major freshwater aquifer in the study area is the Chicot aquifer in southwest Louisiana (Pleistocene deposits), which is designated as a Sole Source Aquifer (USEPA 2024). The Chicot aquifer includes the lower and upper parts of the Chicot aquifer in the east, the "200-foot", "500-foot" and "700-foot" sands in the west, and the thick undifferentiated sand in the center (Lindaman, 2023; Yang et al., 2024). Chicot aquifer is the most heavily pumped aquifer in Louisiana primarily for rice irrigation and industrial use. Significant drawdowns lead to saltwater upconing and encroachment toward pumping wells (Borrok & Broussard, 2016; Lovelace et al., 2004). Rice can become vulnerable to elevated chloride concentrations of irrigated water.

2.3. Salt Deposits

Saltwater is present at depth near the Chicot aquifer base (Lovelace, 1999) and is highly correlated with relatively shallow salt diapirs (Fig. 1 for locations of salt domes). The top depth of salt domes in the study area ranges from 2 to 5,100 meters. 25% of the domes are located at depths less than 400 meters. Additionally, 75% of the domes are at depths shallower than 3,000 meters. Salt deposits began forming during the Jurassic Period (O'Leary & Gottardi, 2020). Evaporation of saltwater left behind extensive Oxfordian salt deposits. Then, salt domes were formed from the plastic flow of deeply buried salt deposits due to sediment loading, growing as sediments accumulated around them (Williamson & Grubb, 2001). The dissolution of these domes contributes to concentrated brine water in deeper geological formations near the domes (Williamson & Grubb, 2001) and may become the major source of saltwater in the Chicot aquifer.

2.4. Faults

Faults in south Louisiana (Fig. 1) are listric faults (Hanor, 1982). Fault offsets typically increase with depth and influence salinity distribution. The Tepetate-Baton Rouge fault system is the most distinct fault system, consisting of a series of faults trending east-west along the northern margin of the south Louisiana salt dome basin (Hanor, 1982; McCulloh & Heinrich, 2013). The fault system acts as a leaky barrier to lateral fluid migration and salinization (Elshall et al., 2013; Pham and Tsai 2017). Moreover, fault movement has been recognized as a significant factor in coastal plain subsidence and land loss (Roberts et al., 2008).

3. Data Sources

3.1. Soil Porewater Chloride Concentrations

Soil water chloride data were collected from the Coastwide Reference Monitoring System (CRMS) of the Louisiana Coastal Protection and Restoration Authority (CPRA). Implemented in 2003 under the Coastal Wetlands Planning, Protection, and Restoration Act (CWPPRA), the CRMS comprises a network of 392 monitoring sites spreading along Louisiana's coast (Cretini et al., 2011). 346 CRMS stations are within the study area shown in Fig. 2. CRMS porewater samples are extracted within a depth of 30 cm to assess the root zone salinity. Soil water chloride concentrations vary between 55 mg/L and 16,700 mg/L.

3.2. Wells and Streamgages Chloride Concentrations

Well locations and streamgages with chloride measurements are shown in Fig. 2. Chloride data in aquifers was collected from 2,110 water wells, and chloride data in river water was collected from 46 streamgages along the Mississippi River and 22 streamgages along the

Atchafalaya River through the USGS National Water Information System (NWIS). Chloride concentrations in aquifers vary between 1 mg/L and 7,100 mg/L. The chloride concentration from Mississippi River streamgages ranges from 0.3 to 17,500 mg/L. Chloride concentration from Atchafalaya River ranges from 0.3 to 860 mg/L. High groundwater chloride values are observed in the Atchafalaya Basin (more than 800 mg/L). For the Mississippi River, seawater intrusion has been observed up to the streamgage at 92 km (river mile 57) from the river mouth. On the other hand, seawater intrusion in the Atchafalaya River is not as extensive as the Mississippi River.

3.3. AEM Resistivity Data

AEM resistivity data were obtained from Hoogenboom et al. (2023) as shown in Fig. 3. The total flight lines in the model domain are about 14,000 km, including flight lines along the Mississippi River and Atchafalaya River. USGS conducted an AEM survey using a fixed-wing time-domain electromagnetic instrument (TEMPEST) from September 2021 to January 2022 as part of a larger data collection effort that extends earlier surveys of the Lower Mississippi River Valley (Minsley et al., 2021). The AEM data provides information on electrical resistivity up to a depth of about 300 m. However, the depth of investigation (DOI) is lower in less resistive areas where groundwater salinity is elevated. In this study, the model base is set to 240 m below the North American Vertical Datum of 1988 (NAVD 88) and uses AEM resistivity values up to the DOI. This depth covers the entire MRVA and most parts of the Chicot aquifer in the vertical direction.

Collocated chloride data and AEM resistivity data within a 75-meter radius are shown in the upper-right inset figure in Fig. 3 for CRMS stations, water wells, and streamgages. There are 17, 62, and 69 collocated locations for CRMS stations, water quality wells, and streamgages,

225 respectively. These data were used to build transformation functions between AEM resistivity and
226 chloride concentration in the following section.
227

228 # 4. Methodology

229 We propose an integrated approach based on Attia & Tsai (2024b) to estimate salinity in
230 south Louisiana using AEM resistivity data, soil porewater salinity, well water quality data, river
231 water quality data, and a lithologic model. The methods and the workflow are shown in Fig. 4. A
232 lithologic model for the MRVA and Chicot aquifer in the study area was derived from Yang et al.
233 (2024). The collocated data established the relationship between chloride concentration and AEM
234 resistivity in coastal wetlands and aquifers. An ordinary kriging method was used to derive a 3D
235 resistivity model. Finally, chloride concentrations were estimated through the resistivity-to-
236 chloride concertation transformation functions. The 3D resistivity model was constructed on the
237 USGS 1-km National Hydrogeologic Grid (NHG) (Clark et al., 2018). This integrated approach is
238 able to differentiate saline water and aquitard (clay) as both exhibit low resistivity values. Details
239 of these methods are presented below.
240

241 ## 4.1. Lithologic and Resistivity Modeling

242 This study adopted the 3D high-resolution lithologic model (Yang et al., 2024) for the
243 AEM resistivity data analysis. The Louisiana lithologic model was developed using more than
244 4,500 wireline geophysical logs and over 104,000 drillers logs to construct 15 hydrogeologic units,
245 including the MRVA and the Chicot aquifer.
246 The horizon-assisted modeling approach (Yang et al., 2024) was adopted to construct a
247 resistivity model that follows the bedding surfaces of MRVA and Chicot aquifer. For resistivity

modeling, the horizon-assisted modeling method comprises three main steps: (1) transforming AEM resistivity data into a non-dipping domain through horizon restoration; (2) generating 3D resistivity models in the non-dipping domain. The domain transformation allows 3D resistivity modeling by correlating transformed resistivity data in the horizontal direction; and (3) reverting the 3D models from the non-dipping domain to the original model domain. The horizon-assisted modeling method is efficient in producing regional-scale subsurface models that condition on dip-varying bedding surfaces. Readers are referred to Yang et al. (2024) for technical details about the horizon-assisted modeling method.

In the non-dipping domain, the resistivity model is constructed by the ordinary kriging method on a stack of 2D layers to produce a 3D model. We applied the ordinary kriging method for 291 layers with 1-meter vertical intervals. Each layer has 63,457 horizontal NHG cells. The 3D resistivity model was completed using parallel computing on a supercomputer at Louisiana State University to tackle computational challenges.

4.2. AEM Resistivity-to-Chloride Concentration Transformation

The scatter plot of nearly collocated mean soil water chloride concentration against AEM resistivity values for the top 2-m soil in wetlands is shown in Fig. 5a. 416 soil water samples from 17 collocated CRMS stations in 2021 are shown in inset Fig. 3. The soil water samples have chloride concentrations between 50 to 5000 mg/L. The best-fit power law for coastal wetland salinity is obtained

$$R = 86.72\ Cl_{\text{wetland}}^{-0.529} \quad (1)$$

where Cl is the chloride concentration (mg/L) and R is the AEM resistivity (ohm.m).

Once coastal wetland salinity is mapped based on equation (1), vegetation type of marshes can be estimated by different ranges of chloride concentration (Carruthers et al., 2023): for freshwater marshes, less than 277 mg/L (greater than 4.4 ohm.m); for intermediate marshes, 277 — 2767 mg/L (1.3 — 4.4 ohm.m); for brackish marshes, 2767 — 9963 mg/L (0.7 — 1.3 ohm.m); and for saline marshes, greater than 9963 mg/L (less than 0.7 ohm.m).

Similarly, the scatter plot of nearly collocated mean groundwater chloride concentration vs. AEM resistivity values for MRVA and Chicot aquifer is shown in Fig. 5b. The best-fit power law for salinity in aquifers is

$$R = 86.49 Cl_{\text{aquifer}}^{-0.374} \quad (2)$$

The chloride concentration in MRVA and Chicot aquifer can be estimated from equation (2). AEM resistivity greater than 10.97 ohm.m corresponds to chloride concentration less than 250 mg/L for freshwater aquifers. The U.S. Environmental Protection Agency has the secondary maximum contaminant level (MCL) of 250 mg/L for chloride in drinking water. Brackish groundwater generally has a dissolved-solids content greater than freshwater but less than seawater. Based on the USGS chloride concentration range between 500 and 5,000 mg/L (corresponding to dissolved solids at concentrations between 1,000 and 10,000 mg/L) for brackish groundwater (Stanton et al., 2017), the AEM resistivity value of 8.46 ohm.m is chosen to be the upper bound for brackish groundwater. AEM resistivity values between those two ranges indicate a transition from fresh groundwater and brackish groundwater. Delineating sand facies from the lithofacies model in advance using a large amount of borehole data (Yang et al. 2024) can significantly decrease the confusion on being clay facies or saltwater sand for low resistivity values.

292 It is noted that correlating chloride samples from water wells collected over decades with
293 recently collected AEM interval resistivity data can be challenging because of different spatial and
294 temporal resolutions. However, this approach can at least provide a general picture of 3D
295 subsurface salinity distribution. The Chicot aquifer and MRVA are heavily pumped mainly for
296 irrigation purposes, and salinity is likely to increase over the years. If an area showed high chloride
297 concentration in the past, the area is likely to have high chloride concentration today.
298 Lastly, this study utilized the chloride concentration and specific conductance data from
299 USGS streamgages of the Mississippi River and the Atchafalaya River to develop a resistivity-to-
300 chloride concentration transformation function for river water (Fig. 5c) as follows.

301 $$R = 2929(Cl_{\text{river}} + 112.8)^{-1} \quad \text{for R} < 20 \text{ ohm. m} \tag{3}$$

302 $$R = 673 Cl_{\text{river}}^{-1} \quad \text{for R} \geq 20 \text{ ohm. m} \tag{4}$$

303 This study applied equations (1)-(4) to transform airborne water resistivity to chloride
304 concentration for the wetlands, aquifers, and rivers. The uncertainty of using equation (1)-(2) to
305 estimate logarithm of R (log(R)) is represented by their corresponding standard deviation of the
306 log(R) residuals, which is 0.58 and 0.98, respectively. For rivers, the uncertainty of using equations
307 (3)-(4) is represented by the standard deviation of the log(R) residuals, which is 0.06 for $R < 20$
308 ohm.m and is 0.08 for $R \geq 20$ ohm.m. The relatively high uncertainty for aquifers is expected
309 because of large study areas and local lithological heterogeneity. The relatively low uncertainty
310 for rivers is due to only the presence of water with minimal influence from suspended sediment.
311

5. Results and Discussions

5.1. Salinity Distribution in Coastal Wetlands

The surficial AEM resistivity distribution for the top 2 meters shown in Fig. 6a indicates the presence of extensive saline water (low resistivity) in the Chenier plain and the Mississippi River deltaic plain. The AEM data also shows distinct freshwater (high resistivity) in the Mississippi River and the Atchafalaya River discharging to the Gulf of Mexico. The resistivity-to-chloride concentration formula in equation (1) enables the estimation of chloride concentration (mg/L) distribution for the coastal wetlands shown in Fig. 6b. Using the salinity ranges in Carruthers et al. (2023), Fig. 6c shows the estimated vegetation type distribution, which is similar to that in Nyman et al. (2022).

The strong correlation between the AEM resistivity-chloride concentration and the vegetation type data (Nyman et al., 2022) in the coastal wetland is shown in Fig. 7. Nyman et al. (2022) mapped Louisiana's coastal marsh vegetation using a helicopter survey in 2021 to identify plant species and marsh types at sample points and use the USGS national land cover dataset (NLCD) and the NOAA regional land cover dataset to create a detailed composite dataset of vegetation distribution. The chloride concentration range for each vegetation type is consistent with those ranges in Carruthers et al. (2023). The surficial AEM resistivity data prove very useful in mapping salinity for wetlands and estimating vegetation types, which have the potential to identify wetland areas at risk of salinity stress and support sustainable land use and conservation strategies for ecosystem management.

5.2. AEM Resistivity Implications for Saltwater Deposition and Intrusion in Chicot Aquifer and MRVA

The lithologic model reveals that south Louisiana is extensively covered by fine grains (Fig. 8a). Nevertheless, high resistivity in the hilly area of southwest Louisiana indicates recharge zones for the Chicot aquifer. The high resistivity with great sand thickness in the upper portion of the Chicot aquifer (Fig. 8b) indicates a large amount of fresh groundwater. The low resistivity in the sand facies near the coast and in the deeper depth indicates the presence of saline water.

5.2.1. Chicot Aquifer

The Chicot aquifer ranges from a thin veneer to more than 160 m (520 ft) thick with an average thickness of about 40 m (135 ft) (Sargent et al., 2004). Groundwater modeling by Yang et al. (2023) reveals that extensive pumping for rice irrigation and industrial use in southwest Louisiana has created two large cones of depression (Fig. 9a). Using the resistivity-to-chloride concentration formula in equation (2), the estimated 3D chloride concentration distribution (Fig. 9b) indicates saltwater intrusion in the Chicot aquifer. Jasechko et al. (2020) show that seawater encroachment in southwest Louisiana can be connected to groundwater level decline in inland areas. The 3D salinity mapping for the Chicot aquifer is unprecedented in scale and spatial detail, aligning with water quality measurements and published maps (Van Biersel et al., 2008; Borrok et al., 2018).

The distributions of AEM resistivity for the Chicot aquifer top, middle, and near the base are shown in Fig. 10a-c. The large area of high resistivity in southwest Louisiana indicates abundant fresh groundwater resources. However, resistivity reduces toward the Chicot aquifer base. High resistivity is also observed in the Chicot aquifer top in the Bird's Foot of the Mississippi

River due to the freshwater discharge to the Gulf. The distributions of estimated chloride concentration at the Chicot aquifer top, middle, and near the base are shown in Fig. 10d-f. Fig. 10g-i show the elevation of the Chicot aquifer top, middle, and near the base. The deposition of salt water near the Chicot aquifer base (Fig. 10f) exhibits a high chloride concentration (greater than 3000 mg/L) as the result of brine produced from the dissolution of salt domes. However, the salinity near the coast in the shallow depth of the Chicot (Fig. 10e) is likely from the Gulf seawater and limits the southern extent of freshwater in the Chicot aquifer (Lovelace, 1999; Lovelace et al., 2004).

The chloride plumes mapped by AEM match the historically high chloride concentration described by Lovelace (1999) and Lovelace et al., (2004). The groundwater budget analysis by Vahdat-Aboueshagh et al. (2021) supports large upward flow and saltwater upconing from the lower part to the upper part of the Chicot aquifer in the east, from the "700-foot" sand to the "500-foot" sand in the west, and in the thick undifferentiated sand in the center. Moreover, lateral seawater intrusion from the Gulf of Mexico toward the centers of the cone of depression is also expected.

It is interesting to observe a distinct tongue of saltwater in the Atchafalaya Basin at the Chicot aquifer top, intruding more than 200 km from the Gulf of Mexico further inland as shown in Fig. 10e. This tongue of saltwater continues upward and has been reported in the MRVA (Smoot, 1986). The forming of this saltwater tongue is likely due to ancient sea level rise with the highest rates of encroachment in the most permeable zone underlying the Atchafalaya Basin (Nyman, 1984). This unique saltwater deposition explains the reason why there are not many pumping wells in the Atchafalaya Basin.

5.2.2. MRVA

Depth to the MRVA varies between 3 m and over 70 m below the land surface. The AEM resistivity distribution and the corresponding estimated chloride concentration using equation (2) for the MRVA top, middle, and base are shown in Fig. 11. Fig. 11g-i show the elevation of the MRVA top, middle, and near the base. The result of the unprecedented 3D salinity mapping for the MRVA matches the water quality data (Van Biersel et al., 2008) and the published water quality maps (Van Biersel et al., 2008; Borrok et al., 2018). The base of the MRVA shows high chloride concentration (greater than 3000 mg/L) in the coastal zone (Fig. 11f). The aforementioned tongue of saltwater (Smoot, 1986) is all the way to the top of MRVA (Fig. 11d), although there are shallow water wells in the fresh and less saline groundwater zones that are predominately for the irrigation purpose (Yang et al., 2023).

5.2.3. Saltwater Stratification in a Complex Aquifer System

The AEM method captures the saltwater stratification in different cross sections shown in Fig. 12. The potentiometric surface of August 2020 shows that the MRVA is a confined aquifer. The Chicot aquifer is also confined except for the northern area ($\overline{AA'}$) including the recharge zone and small parts of the heavily pumped areas ($\overline{DD'}$). The continuous vertical sampling of the AEM data offers a more complete picture of the vertical distribution of saltwater than can be obtained by water quality sampling from wells as it passes from the point data to the regional scale (Gottschalk et al., 2020). The estimated AEM-derived chloride concentrations have good agreement with the measurements from sampled waters. Several wells screened at the MRVA and the Chicot aquifer have exhibited high levels of saline groundwater. It appears that the majority of saltwater in the Chicot aquifer and MRVA originates from deeper depths. Cross sections $\overline{AA'}$ and

402 $\overline{DD'}$ (Fig. 12a, d) indicate the Chicot aquifer to be prolific in southwest Louisiana. Groundwater in
403 the Chicot aquifer appears to be more saline toward the coastal zone. The MRVA and Chicot
404 aquifer are connected as shown in the cross sections, $\overline{BB'}$, $\overline{CC'}$ and $\overline{DD'}$ (Fig. 12b-d). As such,
405 saltwater moves upward from the Chicot aquifer to the MRVA driven by either concentration
406 gradients or anthropogenetic pumping. Extraction of fresh water from shallower depths creates
407 saltwater upconing in both Chicot aquifer and MRVA as shown in these cross sections. Saltwater
408 upconing is a response to the pressure depression around a pumping well, leading to the upward
409 transport of saltwater towards the well and the creation of a transition zone between freshwater
410 and saltwater water.
411
412 **5.3. AEM Data Implications on Fault Traces**
413 This study reveals abrupt chloride changes across some fault traces shown in Fig. 10 and
414 11. This observation indirectly confirms known fault locations and indicates faults as leaky barriers
415 to lateral fluid migration and salinization. However, surficial fault traces in the Atchafalaya Basin
416 and the coastal zone are often missing because of coastal erosion or buried by recent alluvium.
417 Missing fault traces are often estimated from clear offsets of underlying stratigraphy (McCulloh
418 & Heinrich, 2013), bay bottom characteristics in southernmost lakes (Roberts et al., 2008), or
419 vegetation edges. In addition, the AEM resistivity data is able to infer missing fault traces where
420 abrupt chloride changes are observed. For example, the Baton Rouge fault trace, which isn't
421 apparent at the surface in the Atchafalaya Basin (McCulloh & Heinrich, 2013) can be confirmed
422 by the abrupt chloride change in the Chicot aquifer shown in the inset figures in Fig. 10e-f. Such
423 an abrupt chloride change is not obvious in the MRVA because of less fault displacement and
424 lower salinity, compared to the Chicot aquifer.

425

426 **5.4. Salinity Analysis along the Mississippi River and Atchafalaya River**

427 The AEM survey along the Mississippi River, a flight line of nearly 500 km, yielded a
428 high-resolution resistivity profile for both the river and the subsurface shown in Fig. 13a. The
429 timing of the survey coincides with a high likelihood of seawater intrusion into the Mississippi
430 River during the low flow season (November-December). Seawater intrusion occurs when the
431 river's flow falls below a certain level and seawater is able to move upriver from the Gulf. The
432 study utilized the chloride concentration and AEM resistivity data to develop a resistivity-to-
433 chloride concentration transformation function for river water in equations (3)-(4). The result
434 clearly shows seawater intrusion from the Head of Passes (River Mile, RM 0) up to 70 km (RM
435 43) in Fig. 13b. The chloride concentration of the seawater wedge can be higher than 3,000 mg/L.
436 The result aligns with previous significant episodes of seawater intrusion in the Mississippi River,
437 which occurred in 1988, 1999, 2012, 2022, and 2023. Prolonged seawater intrusion can stop water
438 intake systems and deplete freshwater resources. The AEM data is proven to be an effective tool
439 to map the Mississippi River's seawater wedge. Moreover, high resistivity close to the riverbed
440 typically suggests fresh surface water-groundwater interactions through coarse sediments as
441 shown in MRVA in Fig. 13c. Limited surface water-groundwater interaction occurs from 240 km
442 (RM 149) to the Gulf because of thick riverbed clay deposits.

443 The resistivity profile along the Atchafalaya River (230-km flight line) (Fig. 14a) shows
444 similar seawater intrusion from the Gulf up to 17 km (Fig. 14b). Riverbed clay deposits are thin or
445 missing such that seawater can infiltrate into the MRVA and the Chicot aquifer. Additionally, the
446 estimated chloride concentration of the seawater wedge is higher than 3000 mg/L. The Atchafalaya
447 River has good hydraulic connections to the MRVA between 80 km to 220 km from the river

mouth and likely recharges the MRVA and restricts the migration of saltwater from the Chicot aquifer (Fig. 14c).

5.5. Implications

It is noted that the AEM data is representative of the salinity condition at the time of data collection. However, given the slow nature of groundwater movement, it will take decades for significant salinity changes to occur in aquifers. Therefore, the AEM-derived salinity distribution can be regarded as representing the aquifer conditions of past decades. On the other hand, the dynamics of the river-estuary interaction is rapid. The AEM-derived salinity wadge is a snapshot of seawater intrusion in the rivers. It will require frequent AEM surveys to capture temporal salinity variations in rivers and wetlands. Moreover, the distribution of saline water derived from AEM surveys provides a valuable dataset for numerical model development of flow and solute transport.

6. Conclusions

The study integrates airborne electromagnetic (AEM) resistivity data, borehole data, and water quality data to map saltwater in Louisiana's coastal aquifers and wetlands. The salinity maps created from AEM resistivity data align with previously identified saltwater encroachment areas. By converting AEM resistivity to chloride concentration in the coastal wetlands, the study predicts the distribution of salinity-dependent marshes with reasonable accuracy. The good agreement between AEM data and well water quality measurements validates this approach, underscoring the utility of AEM in filling spatial gaps in monitoring wells and tracking freshwater/saltwater interfaces.

AEM resistivity data analysis reveals detailed insights into saltwater intrusion in the Chicot aquifer and MRVA in southern Louisiana. The AEM data confirms the distinct tongue of saltwater that appears in the Chicot aquifer and extends to the MRVA within the Atchafalaya Basin. The AEM data also confirms the fresh groundwater recharge zones of the Chicot aquifer in the hilly areas of southwest Louisiana and shows extensive saltwater presence in deeper depths and near the coast, originating from salt domes and the Gulf of Mexico, respectively. The saltwater stratification and upconing patterns indicate that excessive agricultural and industrial groundwater withdrawals exacerbate saltwater migration from the Chicot aquifer base.

The abrupt chloride changes across previously mapped surficial fault traces confirm known fault locations and suggest their role as leaky barriers to fluid migration and salinization. In areas where surface fault traces are often obscured, such as the Atchafalaya Basin, AEM resistivity data helps to infer these missing traces, such as the Baton Rouge fault. Furthermore, the high-resolution AEM resistivity profiles along the Mississippi River and Atchafalaya River indicate seawater intrusion from the Gulf of Mexico. The seawater wedge encroaches in the Mississippi River and Atchafalaya River. Seawater intrusion into the Mississippi River poses a potential threat to freshwater intakes for public water supply.

The study presents an integrated approach using AEM technology to decipher wetland and aquifer salinization, fault traces, and river seawater intrusion. The findings highlight the complexity of salinization processes within Louisiana's coastal zone. The challenges for sustaining coastal communities persist, as climate change, rising sea levels, and land subsidence are expected to exacerbate saltwater intrusion.

7. Acknowledgments

This study was supported in part by the U.S. Geological Survey under Grant/Cooperative Agreement No. G21AC10765 and the U.S. National Science Foundation (Award No. 2019561). LSU High Performance Computing and LSU Center for Computation & Technology are acknowledged for providing a supercomputer for this study.

8. References

Attia, M., & Tsai, F. T.-C. (2024a). Successive bootstrapping deep learning approach and airborne EM-borehole data fusion to understand salt water in the Mississippi River Valley Alluvial Aquifer. Science of the Total Environment, 932. https://doi.org/10.1016/j.scitotenv.2024.172950

Attia, M., & Tsai, F. T.-C. (2024b). Integrated airborne geophysical data for mapping saltwater in the Mississippi River Valley alluvial Aquifer, northeast Louisiana. Journal of Hydrology, 131877. https://doi.org/10.1016/j.jhydrol.2024.131877

Barbier, E. B., Hacker, S. D., Kennedy, C., Koch, E. W., Stier, A. C., & Silliman, B. R. (2011). The value of estuarine and coastal ecosystem services. Ecological Monographs, 81(2), 169–193. https://doi.org/10.1890/10-1510.1

Baustian, M. M., Stagg, C. L., Perry, C. L., Moss, L. C., Carruthers, T. J. B., & Allison, M. (2017). Relationships Between Salinity and Short-Term Soil Carbon Accumulation Rates from Marsh Types Across a Landscape in the Mississippi River Delta. Wetlands, 37(2), 313–324. https://doi.org/10.1007/s13157-016-0871-3

Beckman, J. D., & Williamson, A. K. (1990). Salt-dome locations in the Gulf Coastal Plain, south-central United States. US Geological Survey Water-Resources Investigations Report

516 90-4060. https://doi.org/10.3133/wri904060
517 Bense, V. F., & Person, M. A. (2006). Faults as conduit-barrier systems to fluid flow in
518 siliciclastic sedimentary aquifers. Water Resources Research 42(5), W05421,
519 doi:10.1029/2005WR004480.
520 Bianchin, M. S., Smith, L., & Beckie, R. D. (2011). Defining the hyporheic zone in a large
521 tidally influenced river. Journal of Hydrology, 406(1-2), 16-29.
522 https://doi.org/10.1016/j.jhydrol.2011.05.056
523 Bilskie, M. V., Hagen, S. C., Medeiros, S. C., & Passeri, D. L. (2014). Dynamics of sea level rise
524 and coastal flooding on a changing landscape. Geophysical Research Letters, 41(3), 927–
525 934. https://doi.org/10.1002/2013GL058759
526 Boano, F., Harvey, J. W., Marion, A., Packman, A. I., Revelli, R., Ridolfi, L., & Wörman, A.
527 (2014). Hyporheic flow and transport processes: Mechanisms, models, and biogeochemical
528 implications. Reviews of Geophysics, 52(4), 603-679. https://doi.org/10.1002/2012RG00
529 Boesch, D. F., Josselyn, M. N., Mehta, A. J., Morris, J. T., Nuttle, W. K., Simenstad, C. A., &
530 Swift, D. J. (1994). Scientific assessment of coastal wetland loss, restoration and
531 management in Louisiana. Journal of Coastal Research, i-103.
532 http://www.jstor.org/stable/25735693
533 Borrok, D. M., & Broussard, W. P. (2016). Long-term geochemical evaluation of the coastal
534 Chicot aquifer system, Louisiana, USA. Journal of Hydrology, 533, 320–331.
535 https://doi.org/10.1016/j.jhydrol.2015.12.022
536 Borrok, D. M., Chen, J., Eldardiry, H., & Habib, E. (2018). A framework for incorporating the
537 impact of water quality on water supply stress: an example from Louisiana, USA. JAWRA
538 Journal of the American Water Resources Association, 54(1), 134-147.

https://doi.org/10.1111/1752-1688.12597

Briggs, M. A., Nelson, N., Gardner, P., Solomon, D. K., Terry, N., & Lane, J. W. (2019). Wetland-scale mapping of preferential fresh groundwater discharge to the Colorado River. Groundwater, 57(5), 737-748. https://doi.org/10.1111/gwat.12866

Carruthers, T., Stagg, C., & Baustian, M. M. (2023). Preparing for future changes: Louisiana's Coast. The Water Institute.

Casarez, I.R. (2020) Aquifer extents in the coastal lowlands aquifer system regional groundwater availability study area in Texas, Louisiana, Mississippi, Alabama, and Florida, U.S. Geological Survey data release, https://doi.org/10.5066/P9BH2KG2.

Clark, B., Barlow, P. M., Peterson, S. M., Hughes, J. D., Reeves, H. W., & Viger, R. J. (2018). National-scale grid to support regional groundwater availability studies and a national hydrogeologic database. U.S. Geological Survey data release. https://doi.org/https://doi.org/10.5066/F7P84B24

Couvillion, B.R., Beck, H., Schoolmaster, D., & Fischer, M. (2017). Land area change in coastal Louisiana 1932 to 2016: U.S. Geological Survey Scientific Investigations Map 3381, 16 p. pamphlet, https://doi.org/10.3133/sim3381.

Craft, C., Clough, J., Ehman, J., Jove, S., Park, R., Pennings, S., Guo, H., & Machmuller, M. (2009). Forecasting the effects of accelerated sea-level rise on tidal marsh ecosystem services. Frontiers in Ecology and the Environment, 7(2), 73–78. https://doi.org/10.1890/070219

Cretini, K.F., Visser, J.M., Krauss, K.W., & Steyer, G.D. (2011). CRMS vegetation analytical team framework—Methods for collection, development, and use of vegetation response variables: U.S. Geological Survey Open-File Report 2011-1097, 60 p.

562 Danielson, J.J., Tyler, D.J., Cushing, W.M., Barras, J.A., Poppenga, S.K. Beverly, S.D, &
563 Shogib, R. (2022) Topobathymetric Model of the Northern Gulf of Mexico, 1885 to 2021:
564 U.S. Geological Survey data release, https://doi.org/10.5066/P99JULDN.
565 Elshall, A.S., Tsai, F. T.-C., & Hanor., J.S. (2013). Indicator Geostatistics for Reconstructing
566 Baton Rouge Aquifer-Fault Hydrostratigraphy, Louisiana, USA. Hydrogeology Journal,
567 21(8), 1731-1747. https://doi.org/10.1007/s10040-013-1037-5
568 Goebel, M., Knight, R., & Halkjær, M. (2019). Mapping saltwater intrusion with an airborne
569 electromagnetic method in the offshore coastal environment, Monterey Bay, California.
570 Journal of Hydrology: Regional Studies, 23, 100602.
571 https://doi.org/10.1016/j.ejrh.2019.100602
572 Gottschalk, I., Knight, R., Asch, T., Abraham, J., & Cannia, J. (2020). Using an airborne
573 electromagnetic method to map saltwater intrusion in the northern Salinas Valley,
574 California. Geophysics, 85(4), B119–B131. https://doi.org/10.1190/geo2019-0272.1
575 Hanor, J. S. (1982). Reactivation of fault movement, Tepetate fault zone, south central
576 Louisiana., Transactions of the Gulf Coast Association of Geological Societies 32, 237-245.
577 Hatch, M., Munday, T., & Heinson, G. (2010). A comparative study of in-river geophysical
578 techniques to define variations in riverbed salt load and aid managing river salinization.
579 Geophysics, 75(4), WA135-WA147. https://doi.org/10.1190/1.3475706
580 Hoogenboom, B.E., Minsley, B.J., James, S.R., & Pace, M.D. (2023). Airborne electromagnetic,
581 magnetic, and radiometric survey of the Mississippi Alluvial Plain, Mississippi Embayment,
582 and Gulf Coastal Plain, September 2021 - January 2022: U.S. Geological Survey data
583 release, https://doi.org/10.5066/P93DO0EO.
584 Jasechko, S., Perrone, D., Seybold, H., Fan, Y., & Kirchner, J. W. (2020). Groundwater level

observations in 250,000 coastal US wells reveal scope of potential seawater intrusion. Nature Communications, 11(1), 1–9. https://doi.org/10.1038/s41467-020-17038-2

Jørgensen, F., Scheer, W., Thomsen, S., Sonnenborg, T. O., Hinsby, K., Wiederhold, H., Schamper, C., Burschil, T., Roth, B., Kirsch, R., & Auken, E. (2012). Transboundary geophysical mapping of geological elements and salinity distribution critical for the assessment of future sea water intrusion in response to sea level rise. Hydrology and Earth System Sciences, 16(7), 1845–1862. https://doi.org/10.5194/hess-16-1845-2012

Kalbus, E., Reinstorf, F., & Schirmer, M. (2006). Measuring methods for groundwater, surface water and their interactions: a review. Hydrology and Earth System Sciences Discussions, 3(4), 1809-1850.

Klassen, J., & Allen, D. M. (2017). Assessing the risk of saltwater intrusion in coastal aquifers. Journal of Hydrology, 551, 730-745. https://doi.org/10.1016/j.jhydrol.2017.02.044

Ladd, D.E., & Travers, L.R. (2019). Generalized regions of the Mississippi Alluvial Plain: U.S. Geological Survey data release, https://doi.org/10.5066/P915ZZQM.

Lane Jr, J. W., Briggs, M. A., Maurya, P. K., White, E. A., Pedersen, J. B., Auken, E., ... & Johnson, C. D. (2020). Characterizing the diverse hydrogeology underlying rivers and estuaries using new floating transient electromagnetic methodology. Science of the Total Environment, 740, 140074. https://doi.org/10.1016/j.scitotenv.2020.140074

Li, S. H., Ge, Z. M., Xie, L. N., Chen, W., Yuan, L., Wang, D. Q., Li, X. Z., & Zhang, L. Q. (2018). Ecophysiological response of native and exotic salt marsh vegetation to waterlogging and salinity: Implications for the effects of sea-level rise. Scientific Reports, 8(1), 1–13. https://doi.org/10.1038/s41598-017-18721-z

Lindaman, M. A. (2023). Hydrogeologic Framework of Southwestern Louisiana. U.S.

608 Geological Survey Scientific Investigations Report, 2023–5004, 31.
609 https://doi.org/https://doi.org/ 10.3133/sir20235004
610 Lovelace, J. K. (1999). Distribution of Saltwater in the Chicot Aquifer System of Southwestern
611 Louisiana, 1995-96. Louisiana Department of Transportation and Development Water
612 Resources Technical Report No. 66, 61 p. https://wise.er.usgs.gov/dp/pdfs/TR66.pdf
613 Lovelace, J.K., Fontenot, J.W., & Frederick, C.P. (2004). Withdrawals, water levels, and specific
614 conductance in the Chicot aquifer system in southwestern Louisiana, 2000-03: U.S.
615 Geological Survey Scientific Investigation Report 2004-5212, 56 p.
616 https://doi.org/10.3133/sir20045212
617 McBride, R. A., Taylor, M. J., & Byrnes, M. R. (2007). Coastal morphodynamics and Chenier-
618 Plain evolution in southwestern Louisiana, USA: A geomorphic model. Geomorphology,
619 88(3–4), 367–422. https://doi.org/10.1016/j.geomorph.2006.11.013
620 McCulloh, R. P., & Heinrich, P. V. (2013). Surface faults of the south Louisiana growth-fault
621 province. Special Paper of the Geological Society of America, 493(January 2013), 37–49.
622 https://doi.org/10.1130/2012.2493(03)
623 Minsley, B.J., Rigby, J.R., James, S.R., et al. (2021). Airborne geophysical surveys of the lower
624 Mississippi Valley demonstrate system-scale mapping of subsurface architecture. Commun
625 Earth Environ 2, 131. https://doi.org/10.1038/s43247-021-00200-z
626 Neubauer, S. C., Franklin, R. B., & Berrier, D. J. (2013). Saltwater intrusion into tidal freshwater
627 marshes alters the biogeochemical processing of organic carbon. Biogeosciences, 10(12),
628 8171–8183. https://doi.org/10.5194/bg-10-8171-2013
629 Nyman, D. J. (1984). The occurrence of high concentrations of chloride in the Chicot aquifer
630 system of southwestern Louisiana. Louisiana Department of Transportation and

631 Development, Water Resources Technical Report No. 33.
632 Nyman, J.A., Reid, C.S., Sasser, C.E., Linscombe, J., Hartley, S.B., Couvillion, B.R., & Villani,
633 R.K. (2022). Vegetation Types in Coastal Louisiana in 2021 (ver. 2.0, April 2023): US
634 Geological Survey data release, https://doi.org/10.5066/P9URYLMS.
635 O'Leary, M., & Gottardi, R. (2020). Relationship between Growth Faults, Subsidence, and Land
636 Loss: An Example from Cameron Parish, Southwestern Louisiana, USA. Journal of Coastal
637 Research, 36(4), 812–827. https://doi.org/10.2112/JCOASTRES-D-19-00108.1
638 Oliver-Cabrera, T., & Wdowinski, S. (2016). InSAR-based mapping of tidal inundation extent
639 and amplitude in Louisiana coastal wetlands. Remote Sensing, 8(5).
640 https://doi.org/10.3390/rs8050393
641 Paine, J. G., Collins, E. W., Nance, H. S., & Niemann, K. L. (2009). Combining airborne
642 electromagnetic induction and hydrochemistry to quantify salinity contributions to a large
643 basin stream, Colorado River, Texas, USA. Near Surface Geophysics, 7(4), 271-282.
644 https://doi.org/10.3997/1873-0604.2009016
645 Panthi, J., Pradhanang, S. M., Nolte, A., & Boving, T. B. (2022). Saltwater intrusion into coastal
646 aquifers in the contiguous United States — A systematic review of investigation approaches
647 and monitoring networks. Science of the Total Environment, 836(April), 155641.
648 https://doi.org/10.1016/j.scitotenv.2022.155641
649 Pham, H.V., & Tsai, F. T.-C. (2017). Modeling complex aquifer systems: a case study in Baton
650 Rouge, Louisiana (USA). Hydrogeology Journal 25(3), 601-615.
651 https://doi.org/10.1007/s10040-016-1532-6
652 Rasmussen, P., Sonnenborg, T. O., Goncear, G., & Hinsby, K. (2013). Assessing impacts of
653 climate change, sea level rise, and drainage canals on saltwater intrusion to coastal aquifer.

654 Hydrology and Earth System Sciences, 17(1), 421–443. https://doi.org/10.5194/hess-17-
655 421-2013
656 Reimann, L., Vafeidis, A. T., & Honsel, L. E. (2023). Population development as a driver of
657 coastal risk: Current trends and future pathways. Cambridge Prisms: Coastal Futures, 1.
658 https://doi.org/10.1017/cft.2023.3
659 Roberts, H. H., Morton, R. A., & Freeman, A. (2008). A High-Resolution Seismic Assessment of
660 Faulting in the Louisiana Coastal Plain. Gulf Coast Association of Geological Societies
661 Transactions, 58(February 2021), 733–745.
662 Sargent, B. P., Frederick, C. P., & Roberts, F. C. (2004). Shallow Sands and Thickness Data for
663 the Chicot Aquifer System Surficial Confining Unit, Southwestern Louisiana. Louisiana
664 Department of Transportation and Development, Water Resources Technical Report No. 22.
665 Saucier, R. T. (1994). Geomorphology and Quaternary geologic history of the Lower Mississippi
666 Valley (Vol. 1). US Army Engineer Waterways Experiment Station.
667 Schiavo, M., Colombani, N., & Mastrocicco, M. (2023). Modeling stochastic saline groundwater
668 occurrence in coastal aquifers. Water Research, 235 (February).
669 https://doi.org/10.1016/j.watres.2023.119885
670 Sengpiel, K. P., & Meiser, P. (1981). Locating the freshwater/salt water interface on the island of
671 Spiekeroog by airborne EM resistivity/depth mapping. Geologisches Jahrbuch C, 29,
672 255-271.
673 Smoot, C. W. (1986). Louisiana hydrologic atlas map no. 2: Areal extent of freshwater in major
674 aquifers of Louisiana. U.S. Geological Survey Water-Resources Investigations Report 86-
675 4150. https://doi.org/10.3133/wri864150
676 Stanton, J. S., Anning, D. W., Brown, C. J., et al. (2017). Brackish Groundwater in the United

States. U.S. Geological Survey Professional Paper 1833. https://pubs.er.usgs.gov/publication/pp1833

Teeple, A.P., Foster, L.K., Lindaman, M.A., Duncan, L.L., and Casarez, I. (2020). Hydrogeologic Data for the Development of the Hydrogeologic Framework of the Coastal Lowlands Aquifer System Regional Groundwater Availability Study Area in Texas, Louisiana, Mississippi, Alabama, and Florida: U.S. Geological Survey data release, https://doi.org/10.5066/P92192WB

USEPA, (2024). Map of Sole Source Aquifer Locations, U.S. Environmental Protection Agency, URL https://www.epa.gov/dwssa/map-sole-source-aquifer-locations

USGS (2004). Salt Diapirs in the Gulf Coast [gcdiapirg]: U.S. Geological Survey data release, https://doi.org/10.5066/P9KH3WB4.

Vahdat-Aboueshagh, H., Tsai, F. T.-C., Bhatta, D., & Paudel, K. P. (2021). Irrigation-Intensive Groundwater Modeling of Complex Aquifer Systems Through Integration of Big Geological Data. Frontiers in Water, 3(April), 1–16. https://doi.org/10.3389/frwa.2021.623476

Van Biersel, T. P., Milner, L. R., & Walden, E. (2008). Development of a chloride standard exceedance map for Louisiana: Gulf Coast Association of Geological Societies Transactions, v. 58, p. 875-881.

Williamson, A. K., & Grubb, H. F. (2001). Ground-water flow in the Gulf Coast aquifer systems, south-central United States, U.S. Geological Survey Professional Paper 1416-F. https://doi.org/10.3133/pp1416F

Yang, S., Tsai, F. T.-C., & Yarbrough, L. D. (2024). Horizon-assisted lithologic modeling: understanding Mississippi Embayment and Coastal Lowlands aquifer systems in Louisiana

and southwestern Mississippi, USA. Hydrogeology Journal, 1-24. https://doi.org/10.1007/s10040-024-02804-z

Yang, S., Tsai, F. T.-C., Bacopoulos, P., & Kees, C. (2023). Comparative analyses of covariance matrix adaption and iterative ensemble smoother on high-dimensional groundwater inverse problems. Journal of Hydrology, 625, 130075. https://doi.org/10.1016/j.jhydrol.2023.130075

Figure Caption:

Figure 1. The study area is in southern Louisiana. The cross-sections $\overline{AA'}$, $\overline{BB'}$, $\overline{CC'}$ and $\overline{DD'}$ are shown in **Fig. 12**. The upper-right inset figure represents the groundwater model domain (Yang et. al., 2023). The geographic landforms, Pleistocene deposits, Chenier plain, Atchafalaya Basin, and Mississippi River deltaic plain, are based on Saucier and Snead (1989) and Saucier (1994). Fault traces are from McCulloh and Heinrich (2013). Salt dome locations are from USGS (2004). Sole Source Aquifers are from the U.S. Environmental Protection Agency (USEPA 2024). The Mississippi River Valley alluvial aquifer (MRVA) extent is determined by Ladd & Travers (2019). The Chicot aquifer extent is from Casarez (2020). The horizontal coordinates (meters) are the USA Albers Equal Area Conic USGS version.

Figure 2. Location of the chloride samples from CRMS stations, USGS streamgages, and chloride wells. CRMS: Coastwide Reference Monitoring System. The horizontal coordinates (meters) are the USA Albers Equal Area Conic USGS version.

Figure 3. The airborne electromagnetic (AEM) resistivity data from Hoogenboom et al. (2023). The inset figures show AEM resistivity profiles for the Mississippi and Atchafalaya Rivers (upper left), the flight lines (lower left), and the nearly collocated CRMS stations, streamgages, and chloride wells with the AEM data (upper right).

Figure 4. The proposed airborne geophysical analysis framework for salinity delineation.

Figure 5. Scatter plots and regression models of the AEM resistivity values vs. measured chloride concentrations at (**a**) nearly collocated CRMS stations for soil porewater and (**b**) nearly collocated USGS groundwater quality wells for MRVA and Chicot aquifer. (**c**) nearly collocated USGS streamgages for the Mississippi River and the Atchafalaya River. The centerline represents the best-fitted power functions as transformation functions. The bandwidth represents one standard deviation of natural log chloride concentration.

Figure 6. (**a**) Surficial (top 2-meter) AEM resistivity distribution, (**b**) estimated chloride concentration by the transformation function (**Fig. 5a**), and (**c**) vegetation types based on the chloride concentration ranges in Carruthers et al. (2023). The horizontal coordinates (meters) are the USA Albers Equal Area Conic USGS version.

Figure 7. AEM resistivity (ohm.m) and estimated chloride concentration (mg/L) ranges for different vegetation types. Vegetation type data is from Nyman et al. (2022).

Figure 8. The lithologic model (Yang et al. 2024) and resistivity model from 2 mbsl (m below the mean sea level) to 240 mbsl: (**a**) 3D aquitards and resistivity distribution in the aquifers, and (**b**) east-west resistivity cross sections. MRVA: The Mississippi River Valley alluvial aquifer. The horizontal coordinates (meters) are the USA Albers Equal Area Conic USGS version. The vertical datum (meters) is NAVD 88.

Figure 9. (a) Groundwater level distribution in August 2020 across the study domain (up to 240 m below land surface), and (**b**) 3D chloride concentration distribution estimated by the transformation function (**Fig. 5b**). Major pumping wells refer to pumping rate greater than 3785 m^3/day (1 million gallon/day). The horizontal coordinates (meters) are the USA Albers Equal Area Conic USGS version.

Figure 10. The AEM resistivity distributions and the corresponding chloride concentration distributions are estimated by the transformation function (**Fig. 5b**) for the Chicot aquifer top,

middle, and near the base. Fault traces are from McCulloh and Heinrich (2013). Salt dome locations are from USGS (2004). The horizontal coordinates (meters) are the USA Albers Equal Area Conic USGS version. The vertical datum (meters) is NAVD 88.

Figure 11. The AEM resistivity distributions and the corresponding chloride concentration distributions are estimated by the transformation function (**Fig. 5b**) for the Mississippi River Valley alluvial aquifer (MRVA) top, middle, and base. Fault traces are from McCulloh and Heinrich (2013). Salt dome locations are from USGS (2004). The horizontal coordinates (meters) are the USA Albers Equal Area Conic USGS version.

Figure 12. The chloride concentration distributions estimated by the transformation function (**Fig. 5b**) and the nearby USGS chloride wells with concentration (mg/L) in parentheses for (**a**) a north-south cross-section $\overline{AA'}$, (**b**) a north-south cross-section $\overline{BB'}$, (**c**) an east-west cross-section $\overline{CC'}$, and (**d**) an east-west cross-section $\overline{DD'}$. The potentiometric surface of August 2020 was derived from Yang et al. (2023). MRVA is the Mississippi River Valley alluvial aquifer. **Fig. 1** shows the location of the cross sections. The horizontal coordinates (meters) are the USA Albers Equal Area Conic USGS version. The vertical datum (meters) is the North American Vertical Datum of 1988 (NAVD 88).

Figure 13. (a) The AEM resistivity profile along the Mississippi River starting at the Head of Passes, (**b**) the estimated river water chloride concentration for the Mississippi River, and (**c**) the estimated chloride concentration in the aquifers. The riverbed elevation was obtained from bathymetric data in Danielson et. al. (2022). The hydrogeologic units were delineated by interpolating the horizon picks in Teeple et al. (2020). MRVA is the Mississippi River Valley alluvial aquifer. The vertical datum for the elevation (meters) is NAVD 88. The cross sections (**a**) and (**c**) have a vertical-to-horizontal (V/H) ratio of 1:600 and (**b**) has a V/H ratio of 1:1200.

Figure 14. (a) The AEM resistivity profile along the Atchafalaya River starting at the river mouth of the Lower Atchafalaya River, (**b**) the estimated river water chloride concentration for the Atchafalaya River, and (**c**) the estimated chloride concentration in the aquifers. The riverbed elevation was obtained from bathymetric data in Danielson et. al. (2022). The hydrogeologic units were delineated by interpolating the horizon picks in Teeple et al. (2020). MRVA is the Mississippi River Valley alluvial aquifer. The vertical datum for the elevation (meters) is NAVD 88. The cross sections (**a**) and (**c**) have a vertical-to-horizontal (V/H) ratio of 1:300 and (**b**) has a V/H ratio of 1:600.

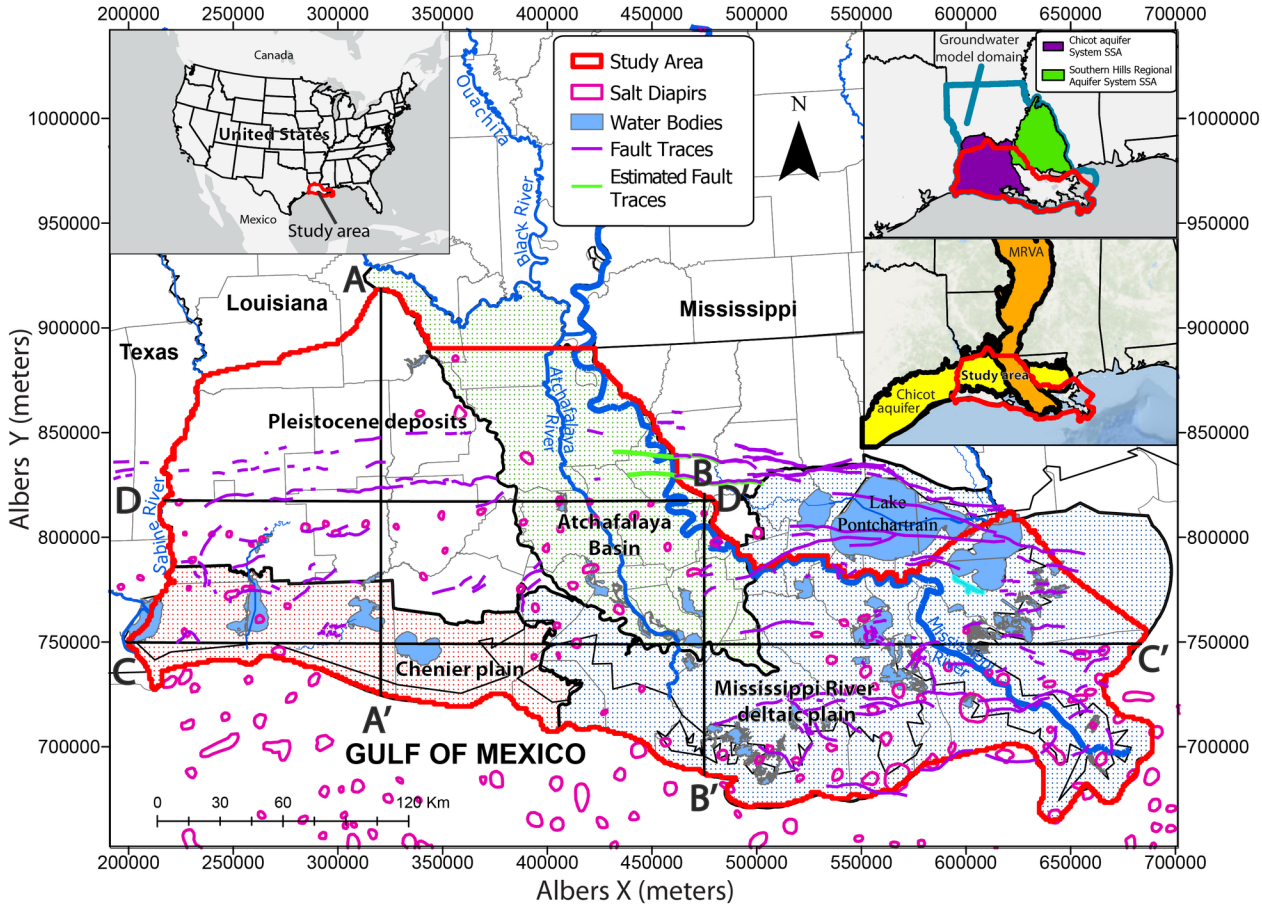
Study Area
Salt Diapirs
Water Bodies
Fault Traces
Estimated Fault Traces
N
Canada
United States
Mexico
Study area
Groundwater model domain
Chicot aquifer System SSA
Southern Hills Regional Aquifer System SSA
MRVA
Study area
Chicot aquifer
Louisiana
Texas
Mississippi
Ouachita
Black River
Atchafalaya River
Sabine River
Pleistocene deposits
Atchafalaya Basin
Lake Pontchartrain
Chenier plain
Mississippi River deltaic plain
GULF OF MEXICO
A
A′
B
B′
C
C′
D
D′
0 30 60 120 Km
200000 250000 300000 350000 400000 450000 500000 550000 600000 650000 700000
1000000 950000 900000 850000 800000 750000 700000
Albers Y (meters)
Albers X (meters)

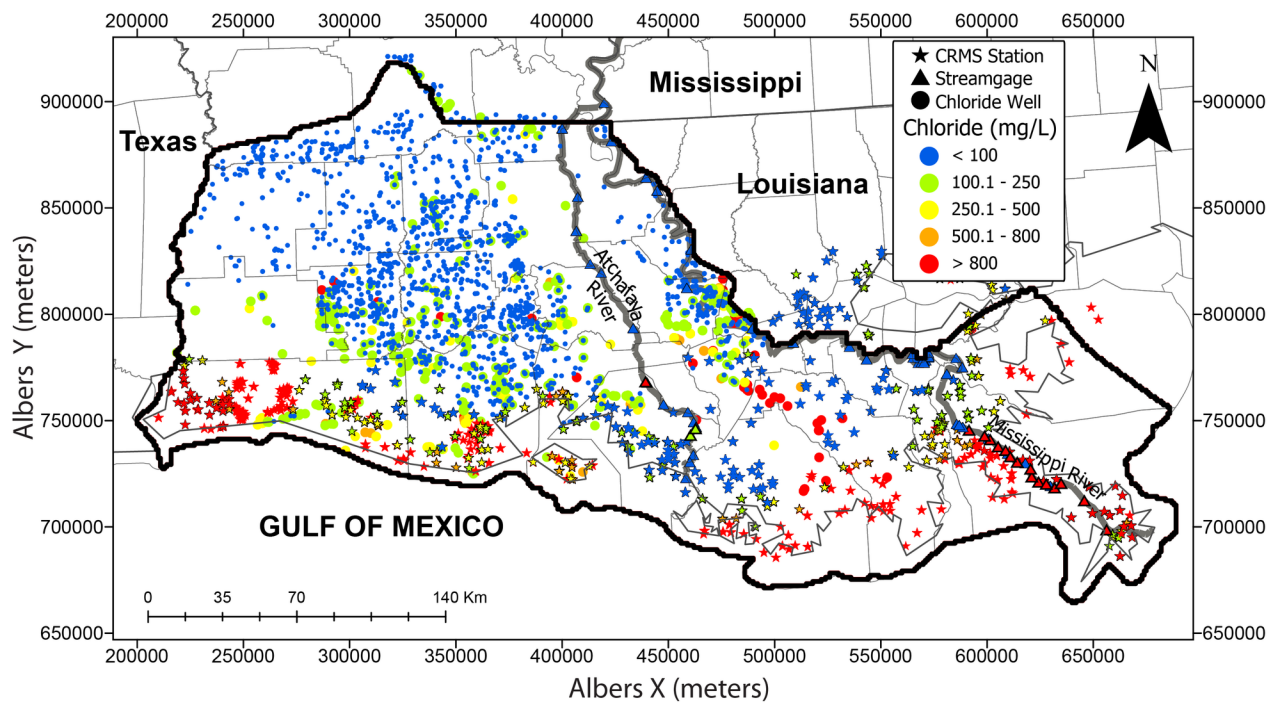
Texas
Mississippi
Louisiana
GULF OF MEXICO
Atchafalaya River
Mississippi River
CRMS Station
Streamgage
Chloride Well
Chloride (mg/L)
< 100
100.1 - 250
250.1 - 500
500.1 - 800
> 800
N
0
35
70
140 Km
200000
250000
300000
350000
400000
450000
500000
550000
600000
650000
900000
850000
800000
750000
700000
650000
Albers Y (meters)
Albers X (meters)

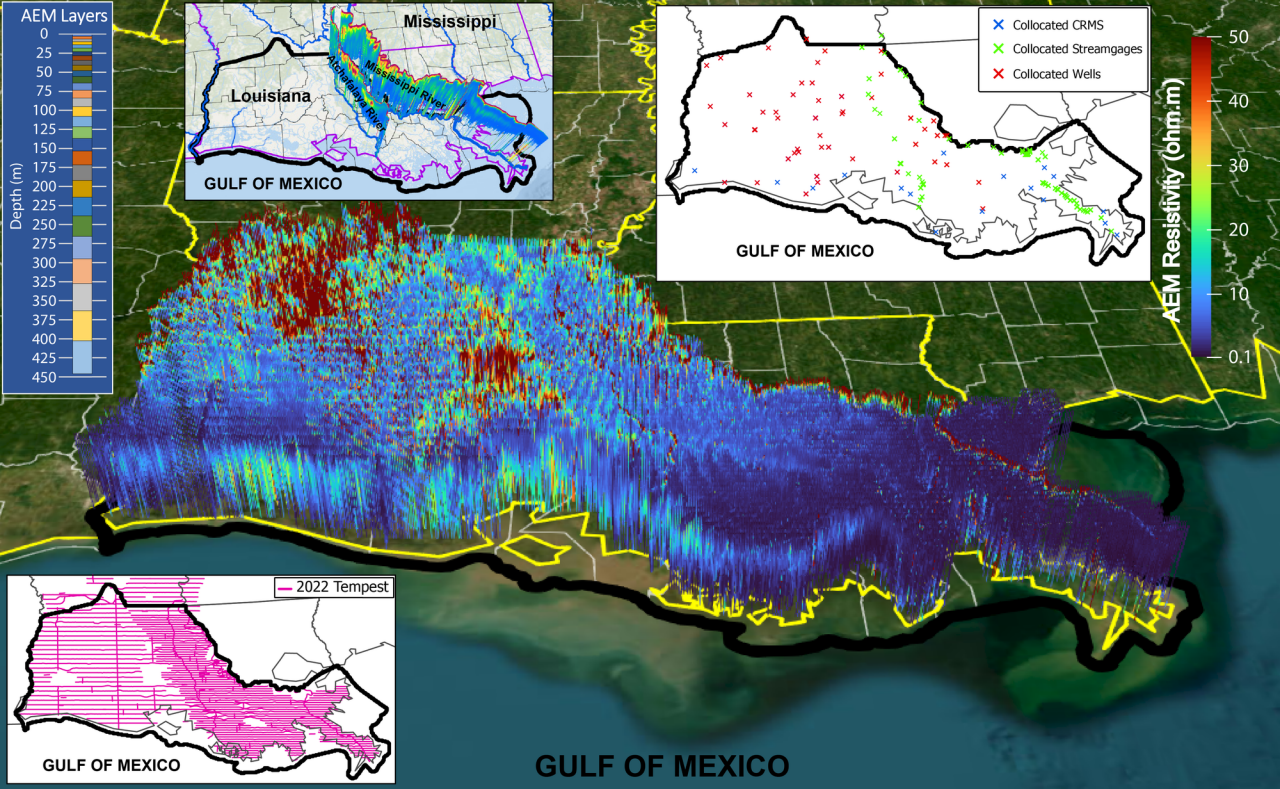
AEM Layers
0
25
50
75
100
125
150
175
200
225
250
275
300
325
350
375
400
425
450
Depth (m)
Mississippi
Louisiana
Mississippi River
Atchafalaya River
GULF OF MEXICO
Collocated CRMS
Collocated Streamgages
Collocated Wells
GULF OF MEXICO
AEM Resistivity (ohm.m)
50
40
30
20
10
0.1
2022 Tempest
GULF OF MEXICO
GULF OF MEXICO

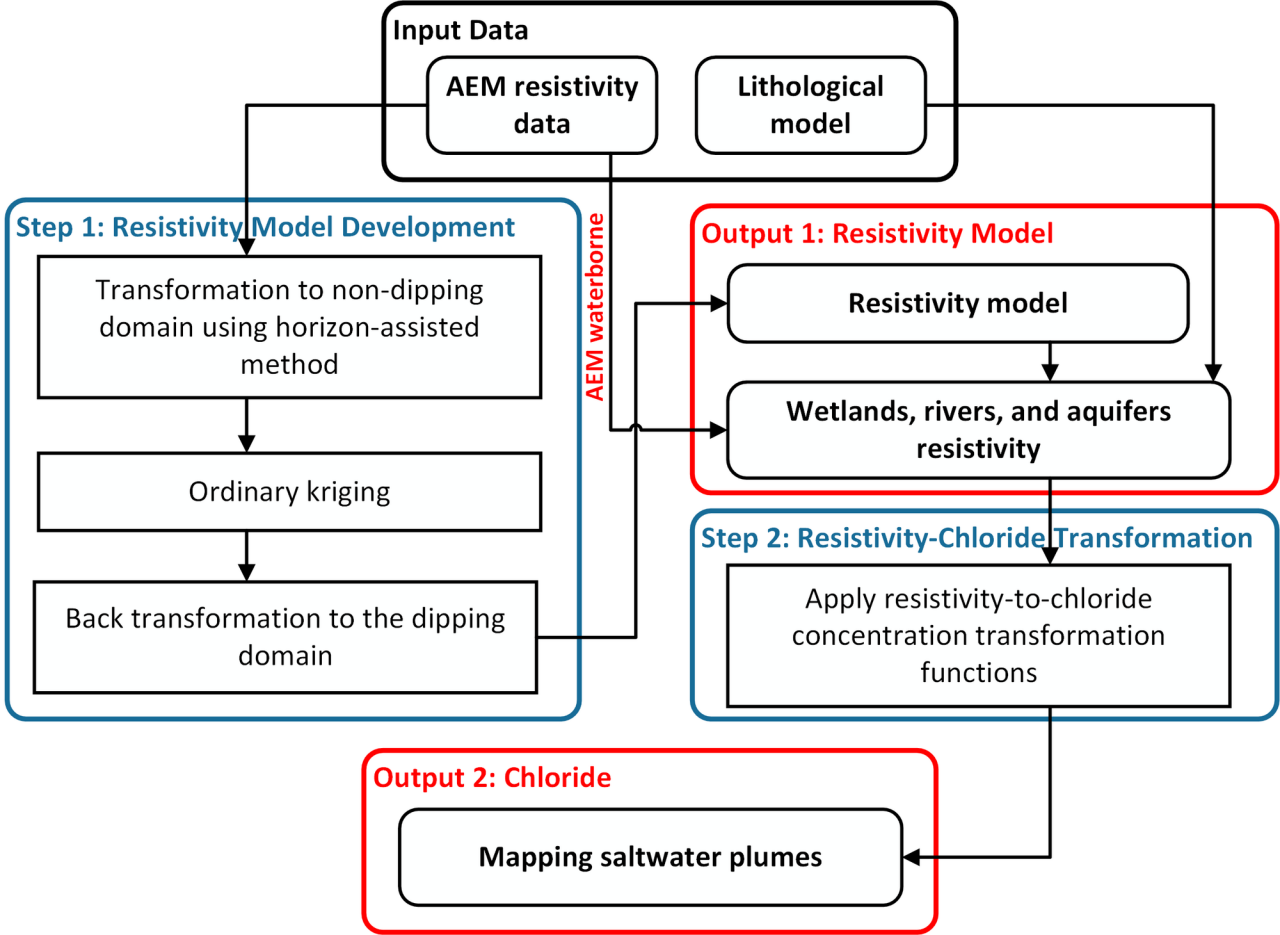
Input Data
AEM resistivity data
Lithological model
Step 1: Resistivity Model Development
Transformation to non-dipping domain using horizon-assisted method
Ordinary kriging
Back transformation to the dipping domain
AEM waterborne
Output 1: Resistivity Model
Resistivity model
Wetlands, rivers, and aquifers resistivity
Step 2: Resistivity-Chloride Transformation
Apply resistivity-to-chloride concentration transformation functions
Output 2: Chloride
Mapping saltwater plumes

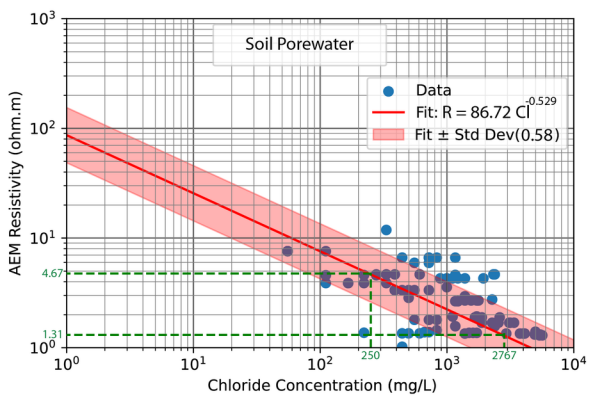
Soil Porewater
Data
Fit: R = 86.72 Cl^-0.529
Fit ± Std Dev(0.58)
AEM Resistivity (ohm.m)
Chloride Concentration (mg/L)
4.67
1.31
250
2767

(a)

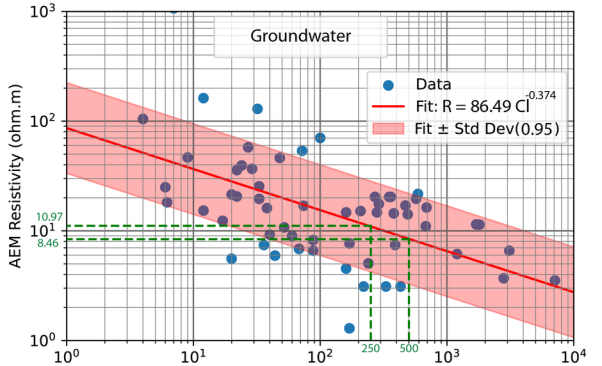
Groundwater
Data
Fit: R = 86.49 Cl^-0.374
Fit ± Std Dev(0.95)
AEM Resistivity (ohm.m)
Chloride Concentration (mg/L)
10.97
8.46
250
500

(b)

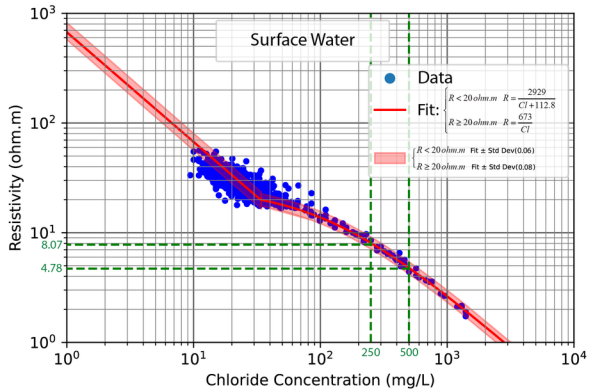
Surface Water
Data
Fit:
R < 20 ohm.m R = 2929 / Cl + 112.8
R ≥ 20 ohm.m R = 673 / Cl
R < 20 ohm.m Fit ± Std Dev(0.06)
R ≥ 20 ohm.m Fit ± Std Dev(0.08)
Resistivity (ohm.m)
Chloride Concentration (mg/L)
8.07
4.78
250
500

(c)

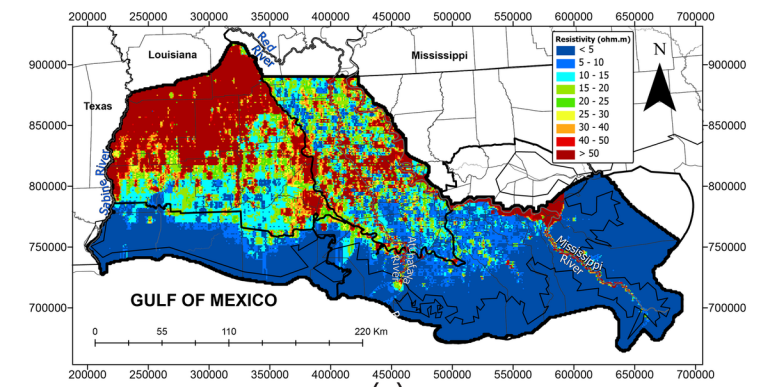

(a)

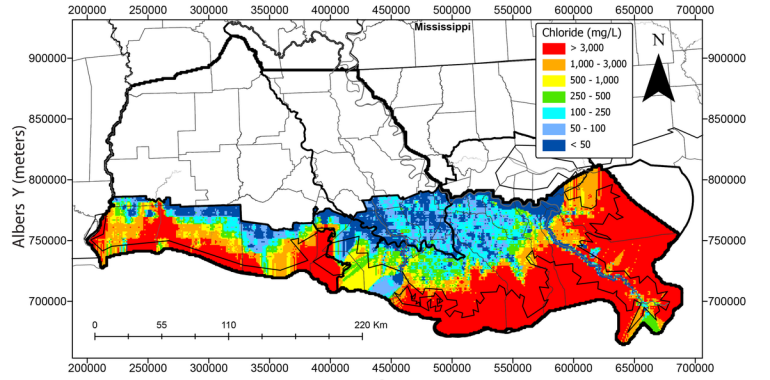

(b)

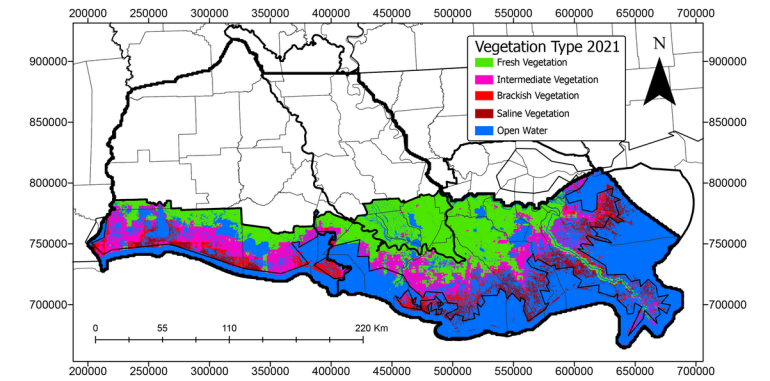

(c)

Albers X (meters)

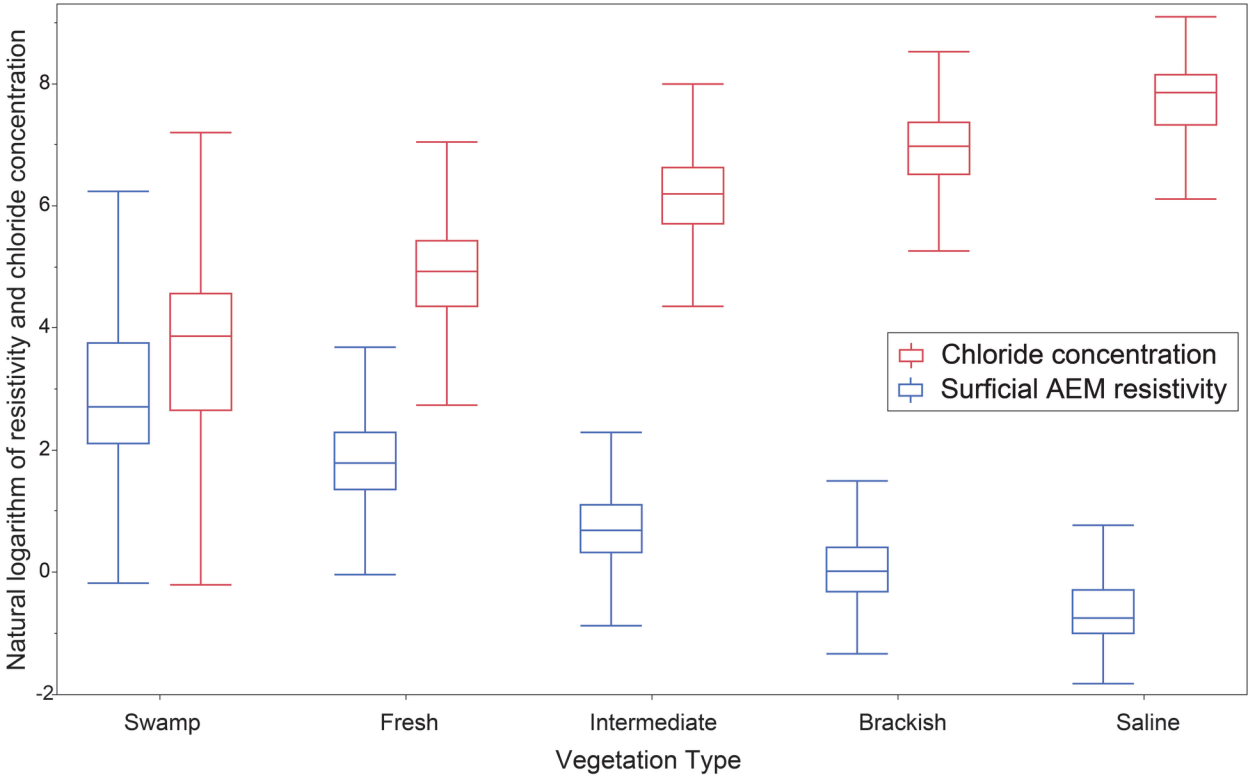
Natural logarithm of resistivity and chloride concentration
8
6
4
2
0
-2
Chloride concentration
Surficial AEM resistivity
Swamp
Fresh
Intermediate
Brackish
Saline
Vegetation Type

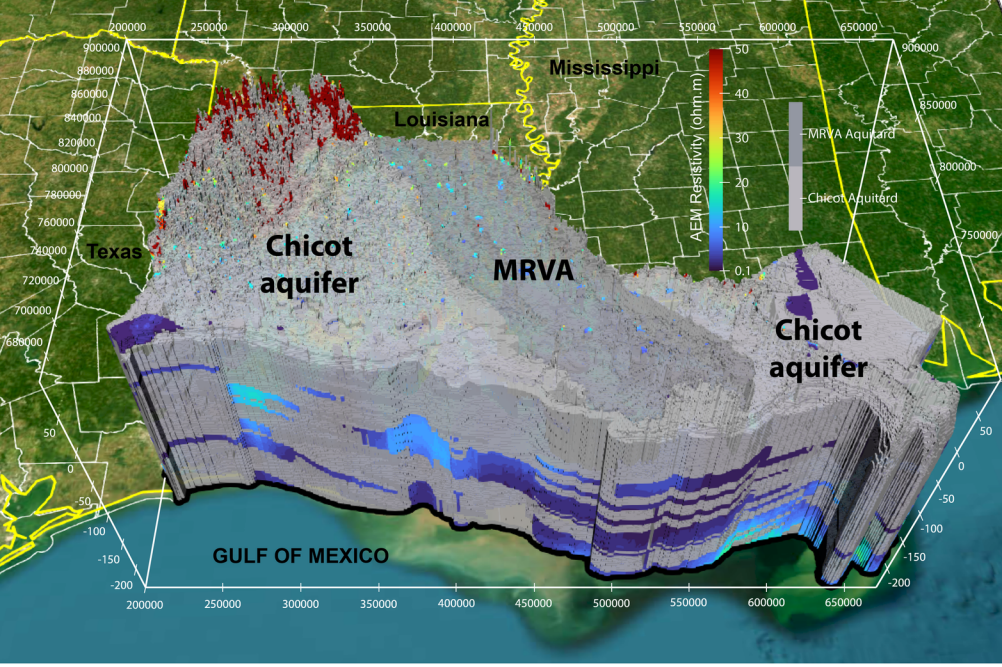
Mississippi
Louisiana
Texas
Chicot aquifer
MRVA
Chicot aquifer
GULF OF MEXICO
AEM Resistivity (ohm.m)
MRVA Aquitard
Chicot Aquitard

(a)

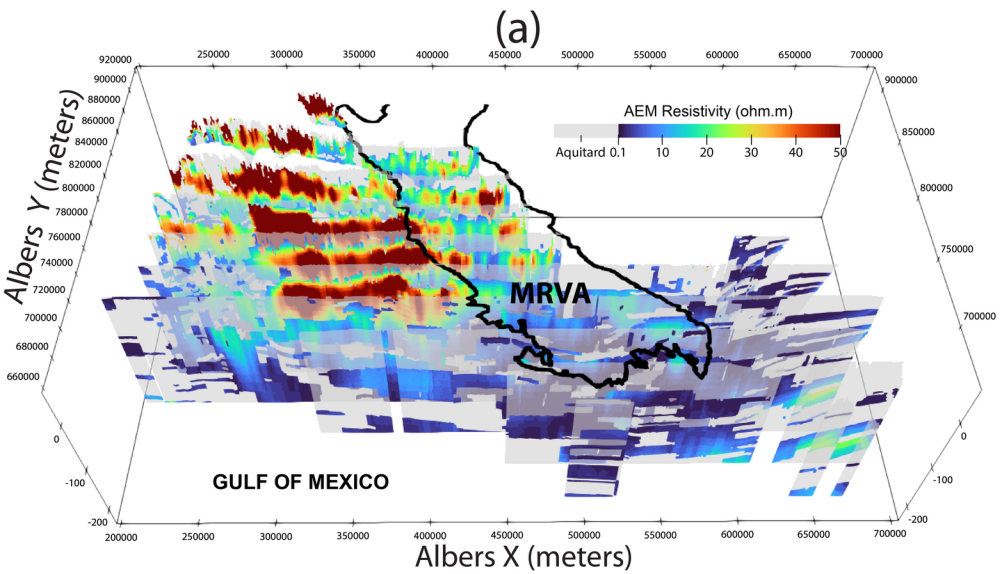
AEM Resistivity (ohm.m)
Aquitard 0.1
10
20
30
40
50
MRVA
GULF OF MEXICO
Albers Y (meters)
Albers X (meters)

(b)

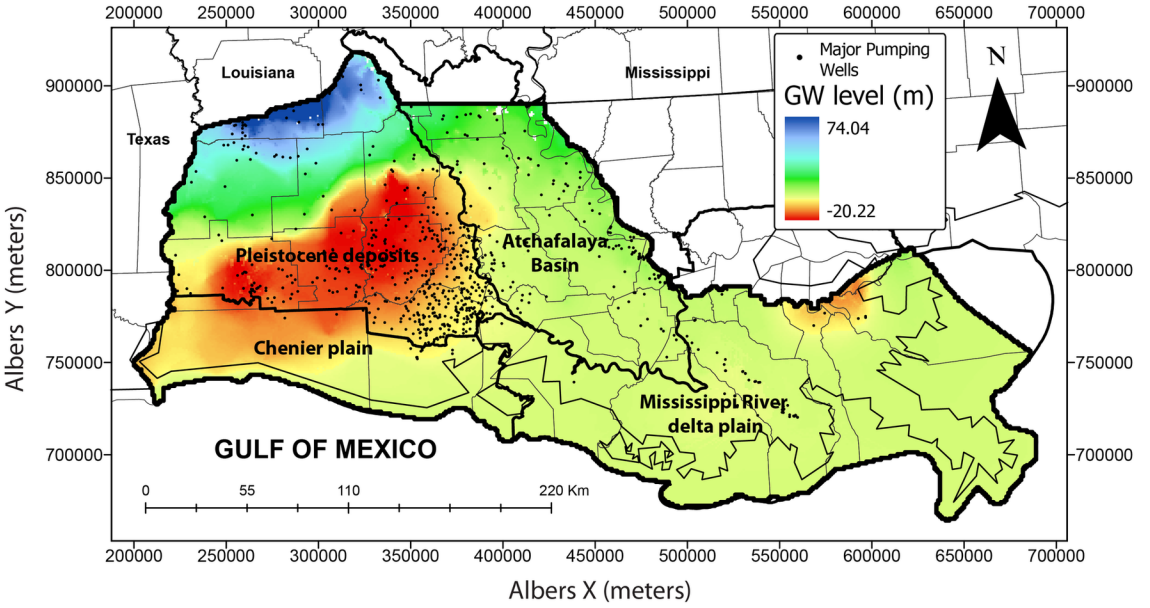
Major Pumping Wells
GW level (m)
74.04
-20.22
N
Louisiana
Mississippi
Texas
Pleistocene deposits
Atchafalaya Basin
Chenier plain
Mississippi River delta plain
GULF OF MEXICO
0
55
110
220 Km
Albers Y (meters)
Albers X (meters)
200000
250000
300000
350000
400000
450000
500000
550000
600000
650000
700000
900000
850000
800000
750000
700000

(a)

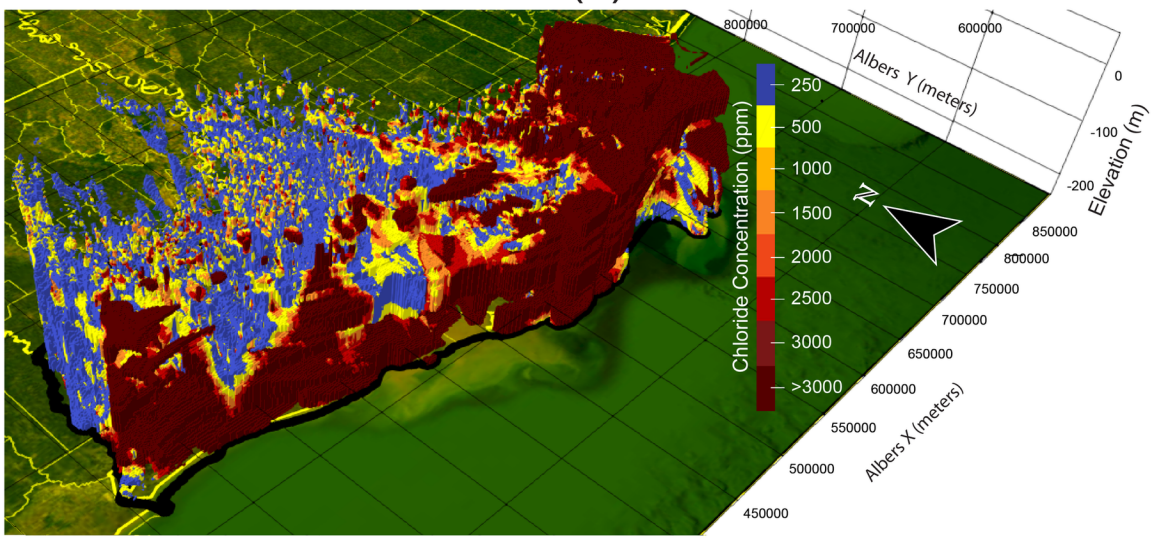
Chloride Concentration (ppm)
250
500
1000
1500
2000
2500
3000
>3000
N
Albers Y (meters)
Albers X (meters)
Elevation (m)
800000
700000
600000
0
-100
-200
850000
800000
750000
700000
650000
600000
550000
500000
450000

(b)

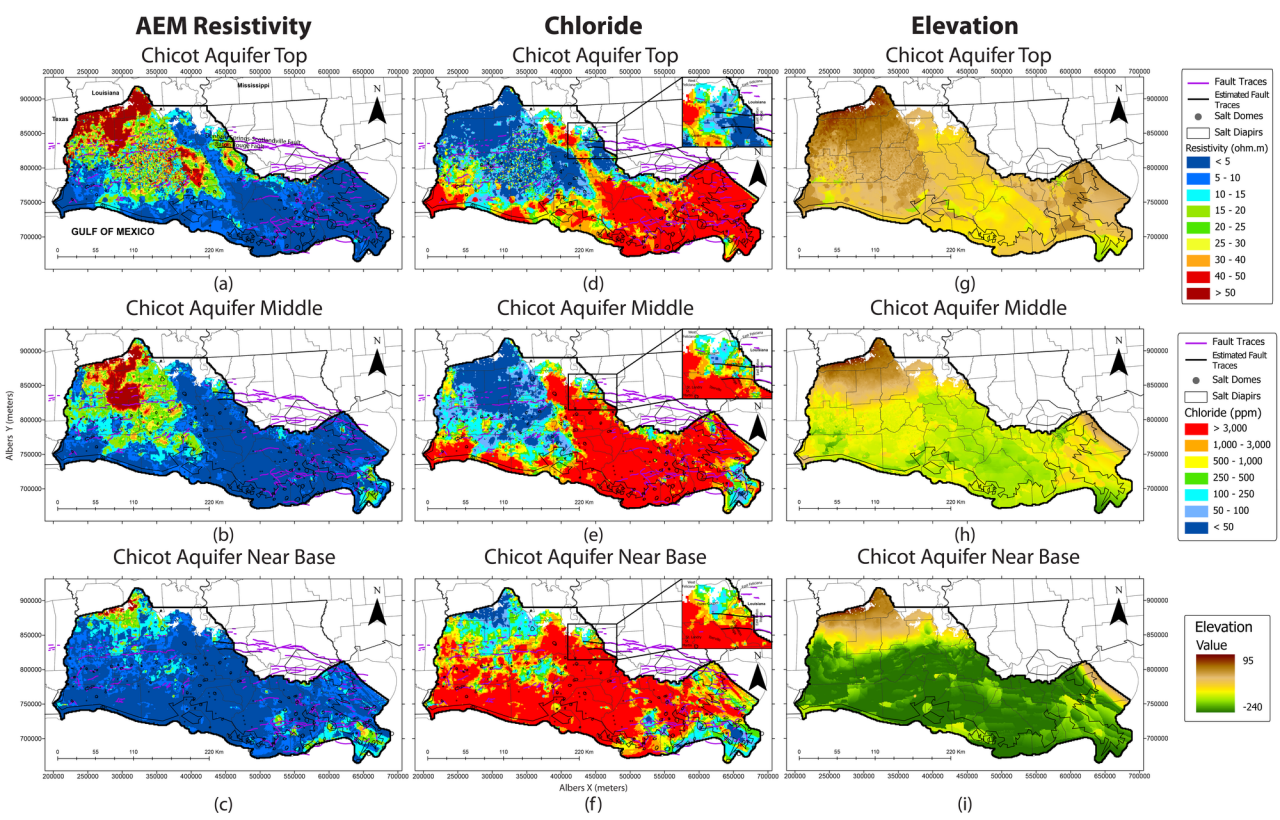
AEM Resistivity
Chloride
Elevation
Chicot Aquifer Top
Chicot Aquifer Middle
Chicot Aquifer Near Base
Louisiana
Mississippi
Texas
GULF OF MEXICO
(a)
(b)
(c)
(d)
(e)
(f)
(g)
(h)
(i)
Albers Y (meters)
Albers X (meters)
Fault Traces
Estimated Fault Traces
Salt Domes
Salt Diapirs
Resistivity (ohm.m)
< 5
5 - 10
10 - 15
15 - 20
20 - 25
25 - 30
30 - 40
40 - 50
> 50
Chloride (ppm)
> 3,000
1,000 - 3,000
500 - 1,000
250 - 500
100 - 250
50 - 100
< 50
Elevation Value
95
-240

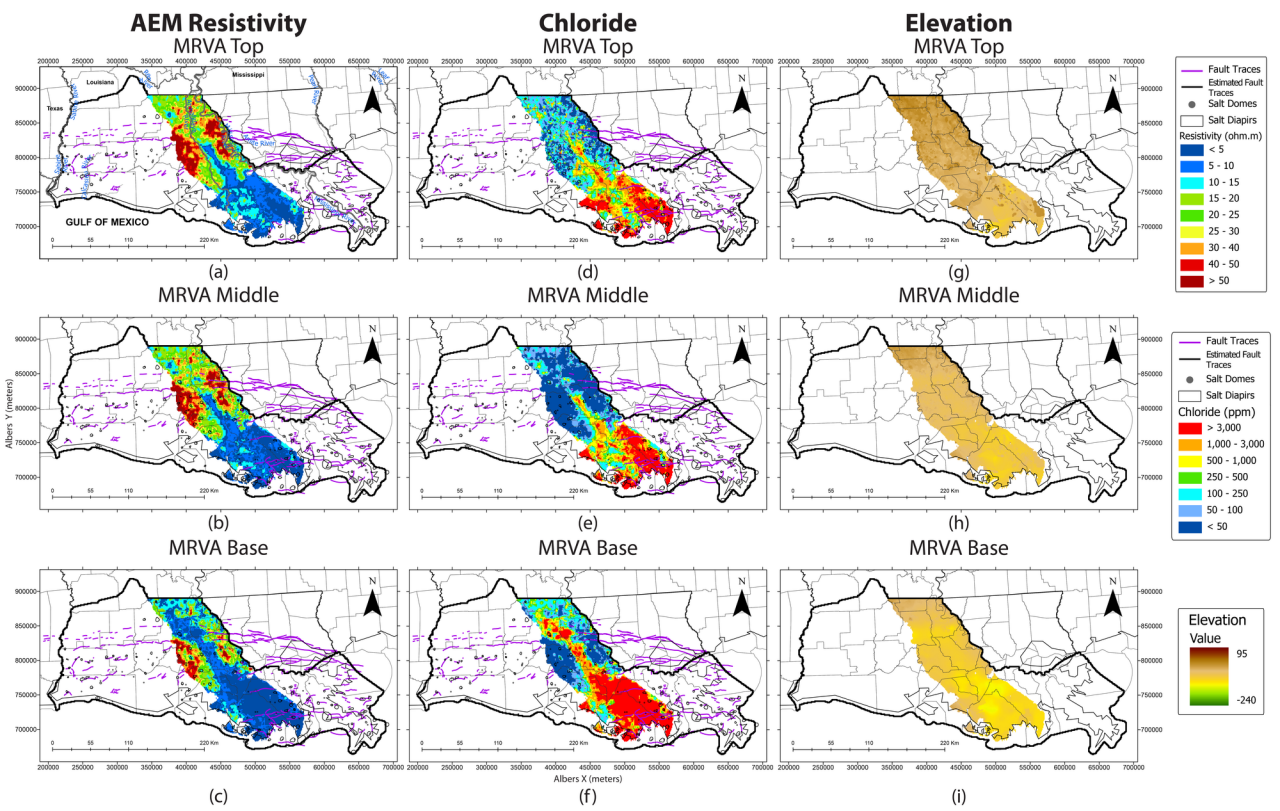
AEM Resistivity
Chloride
Elevation
MRVA Top
MRVA Middle
MRVA Base
Louisiana
Mississippi
Texas
GULF OF MEXICO
Red River
Sabine River
Albers X (meters)
Albers Y (meters)
Fault Traces
Estimated Fault Traces
Salt Domes
Salt Diapirs
Resistivity (ohm.m)
< 5
5 - 10
10 - 15
15 - 20
20 - 25
25 - 30
30 - 40
40 - 50
> 50
Chloride (ppm)
> 3,000
1,000 - 3,000
500 - 1,000
250 - 500
100 - 250
50 - 100
< 50
Elevation
Value
95
-240
(a)
(b)
(c)
(d)
(e)
(f)
(g)
(h)
(i)

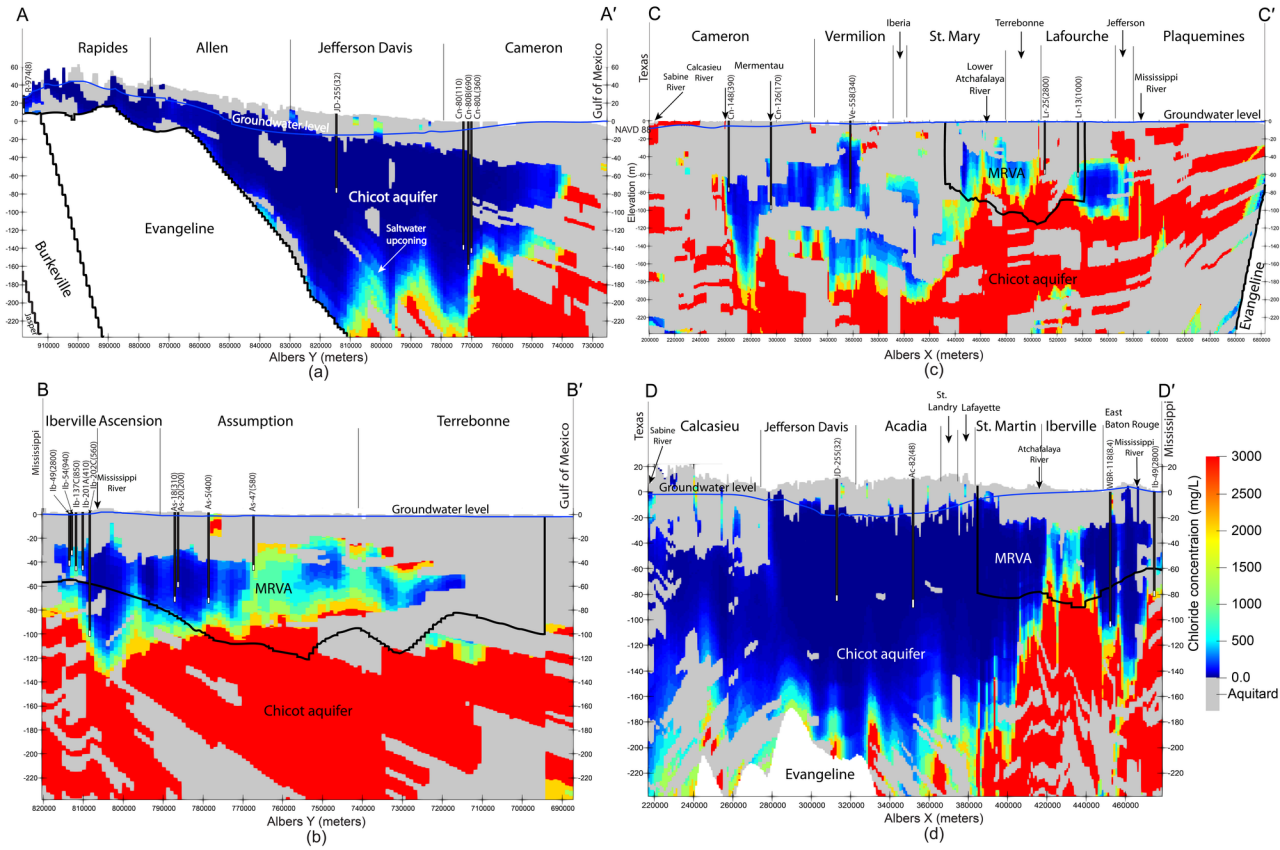
A
A′
Rapides
Allen
Jefferson Davis
Cameron
Gulf of Mexico
Groundwater level
Chicot aquifer
Evangeline
Burkeville
Saltwater upconing
Albers Y (meters)
(a)
C
C′
Cameron
Vermilion
Iberia
St. Mary
Terrebonne
Lafourche
Jefferson
Plaquemines
Texas
Sabine River
Calcasieu River
Mermentau
Lower Atchafalaya River
Mississippi River
Groundwater level
NAVD 88
Elevation (m)
MRVA
Chicot aquifer
Evangeline
Albers X (meters)
(c)
B
B′
Iberville
Ascension
Assumption
Terrebonne
Mississippi
Gulf of Mexico
Mississippi River
Groundwater level
MRVA
Chicot aquifer
Albers Y (meters)
(b)
D
D′
Texas
Sabine River
Calcasieu
Jefferson Davis
Acadia
St. Landry
Lafayette
St. Martin
Iberville
East Baton Rouge
Mississippi
Atchafalaya River
Mississippi River
Groundwater level
MRVA
Chicot aquifer
Evangeline
Albers X (meters)
(d)
Chloride concentraion (mg/L)
3000
2500
2000
1500
1000
500
0.0
Aquitard

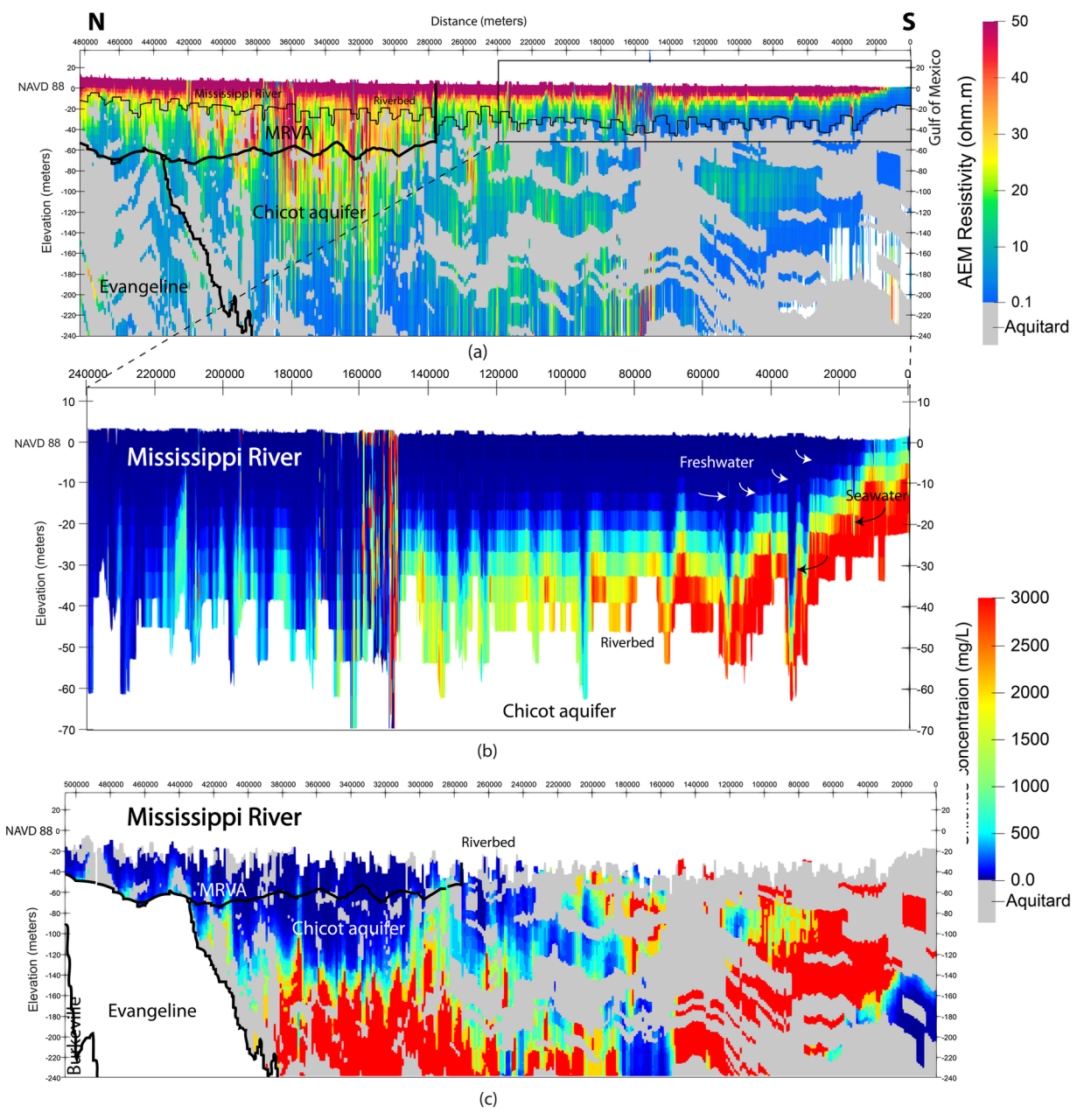
N
Distance (meters)
S
NAVD 88
Mississippi River
Riverbed
MRVA
Chicot aquifer
Evangeline
Gulf of Mexico
Elevation (meters)
AEM Resistivity (ohm.m)
50
40
30
20
10
0.1
Aquitard
(a)
Mississippi River
Freshwater
Seawater
Riverbed
Chicot aquifer
(b)
Concentraion (mg/L)
3000
2500
2000
1500
1000
500
0.0
Aquitard
Mississippi River
Riverbed
MRVA
Chicot aquifer
Evangeline
Baskerville
(c)

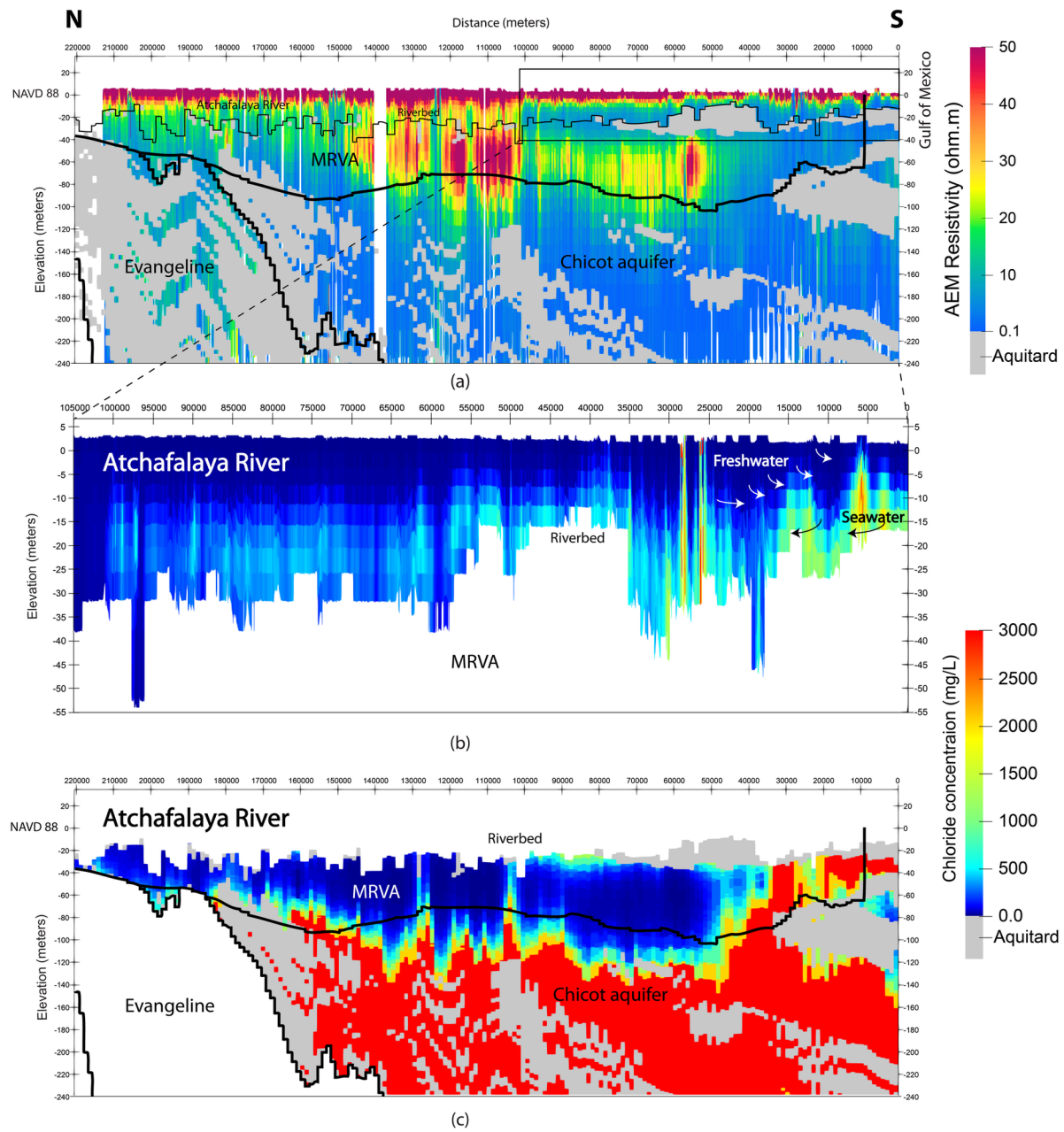
N
Distance (meters)
S
NAVD 88
Atchafalaya River
Riverbed
MRVA
Gulf of Mexico
Elevation (meters)
Evangeline
Chicot aquifer
AEM Resistivity (ohm.m)
50
40
30
20
10
0.1
Aquitard
(a)
Atchafalaya River
Freshwater
Seawater
Riverbed
MRVA
Elevation (meters)
Chloride concentraion (mg/L)
3000
2500
2000
1500
1000
500
0.0
Aquitard
(b)
Atchafalaya River
NAVD 88
Riverbed
MRVA
Elevation (meters)
Evangeline
Chicot aquifer
(c)

AEM Data

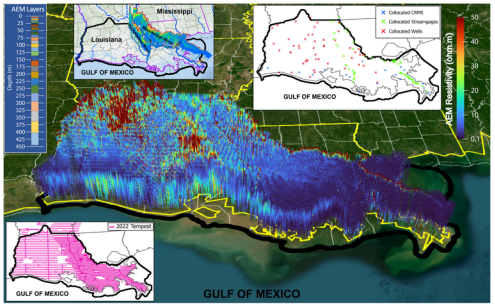

Water Quality Data

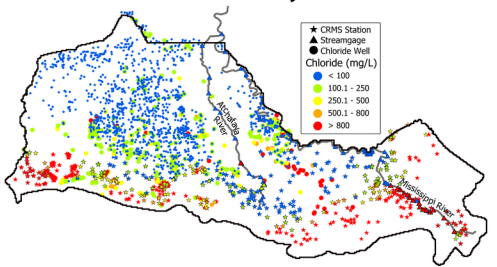

3D Lithological Model with AEM Resistivity Distribution

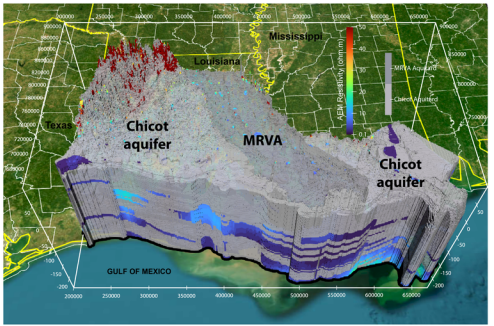

East-West Resistivity Cross Sections